Title

Optical Coherence Tomographic Optic Nerve Head Morphology in Myopia III: The Exposed Neural Canal Region in Healthy Eyes-Implications for High Myopia.

Authors

Hong, Seungwoo
Yang, Hongli
Gardiner, Stuart
et al.

Publication Date

2024-02-01

DOI

10.1016/j.ajo.2023.08.012

Peer reviewed

HHS Public Access

Author manuscript

Am J Ophthalmol. Author manuscript; available in PMC 2025 February 01.

Published in final edited form as:

Am J Ophthalmol. 2024 February ; 258: 55–75. doi:10.1016/j.ajo.2023.08.012.

OCT Optic Nerve Head Morphology in Myopia III: The Exposed Neural Canal Region in Healthy Eyes – Implications for High Myopia

Seungwoo Hong, MD, PhD[1,2,*], **Hongli Yang, PhD**[1,*], **Stuart K Gardiner, PhD**[3], **Haomin Luo, MD**[1,4], **Glen P. Sharpe, MSc**[5], **Joseph Caprioli, MD**[6], **Shaban Demirel, OD, PhD**[3], **Christopher A. Girkin, MD, MSPH**[7], **Christian Y. Mardin, MD**[8], **Harry A. Quigley, MD**[9], **Alexander F. Scheuerle, MD**[10], **Brad Fortune, OD, PhD**[3], **Anuwat Jiravarnsirikul, MD**[1,11], **Camila Zangalli, MD, MPH, PhD**[12], **Balwantray C. Chauhan, Ph.D**[5], **Claude F. Burgoyne, MD**[1]

[1]Devers Eye Institute, Optic Nerve Head Research Laboratory, Legacy Research Institute, Portland, OR, USA

[2]Yebon Eye Clinic, Seoul, Korea.

[3]Devers Eye Institute, Discoveries in Sight Research Laboratories, Legacy Research Institute, Portland, OR 97208-3950, USA

[4]Department of Ophthalmology, Hunan Provincial People's Hospital, Hunan Normal University, Changsha, Hunan Province, P.R.China.

[5]Ophthalmology and Visual Sciences, Dalhousie University, Halifax, NS, Canada

[6]Jules Stein Eye Institute, David Geffen School of Medicine at UCLA, Los Angeles, CA, USA

[7]Department of Ophthalmology, School of Medicine, University of Alabama at Birmingham, Birmingham, Alabama, United States.

[8]Department of Ophthalmology, University of Erlangen, Erlangen, Germany.

[9]Wilmer Eye Institute, Johns Hopkins University, Baltimore, MD, USA

[10]Department of Ophthalmology, University of Heidelberg, Heidelberg, Germany

[11]Department of Ophthalmology, Faculty of Medicine Siriraj Hospital, Mahidol University, Bangkok, Thailand

[12]Department of Glaucoma, Hospital de Olhos Niteroi, Rio de Janeiro, Brazil

Abstract

Corresponding Author: Claude F. Burgoyne, MD, Director, Optic Nerve Head Research Laboratory, Devers Eye Institute, Legacy Research Institute 1225 NE 2nd Ave Portland, OR 97208-3950, cfburgoyne@deverseye.org. **Email Address for reprints:** Claude F. Burgoyne, MD, cfburgoyne@deverseye.org, Optic Nerve Head Research Laboratory, Devers Eye Institute, Legacy Research Institute.
*Seungwoo Hong and Hongli Yang are Co-First-Authors of this paper.

Purpose: To determine the prevalence and magnitude of OCT exposed neural canal (ENC), externally oblique choroidal border tissue (EOCBT), and exposed scleral flange (ESF) regions in 362 non-highly myopic (spherical equivalent −6.00 to 5.75 diopters) eyes of 362 healthy subjects.

Design: Cross-sectional study

Methods: After OCT optic nerve head (ONH) imaging, Bruch's membrane opening (BMO), the anterior scleral canal opening (ASCO), and the scleral flange opening (SFO) were manually segmented. BMO, ASCO and SFO points were projected to BMO reference plane. The direction and magnitude of BMO/ASCO offset as well as the magnitude of ENC, EOCBT and ESF was calculated within 30° sectors relative to the Foveal-BMO axis. Hi-ESF eyes demonstrated an ESF ≥ 100 μms in at least one sector. Sectoral perineural canal choroidal thickness (pNC-CT) was measured and correlations between the magnitude of sectoral ESF and proportional pNC-CT were assessed.

Results: Seventy-three Hi-ESF (20.2%) and 289 Non-Hi-ESF eyes (79.8%) were identified. BMO/ASCO offset, as well as ENC, EOCBT and ESF prevalence and magnitude were greatest inferior temporally where pNC-CT was thinnest. Among Hi-ESF eyes, the magnitude of each ENC region correlated with BMO/ASCO offset magnitude and the sectors with the longest ESF correlated with the sectors with proportionally thinnest pNC-CT.

Conclusions: ONH BMO/ASCO offset, either as a cause or result of ONH neural canal remodeling, corresponds with the sectoral location of maximum ESF and minimum pNC-CT in non-highly myopic eyes. Longitudinal studies to characterize the development and clinical implications of ENC Hi-ESF regions in non-highly myopic and highly myopic eyes are indicated.

Precis

In this report we introduce the scleral flange opening (SFO), a new, deep OCT optic nerve head (ONH) neural canal anatomic landmark and manually segment it, along with Bruch's membrane opening (BMO) and the anterior scleral canal opening (ASCO) in 362 non-highly myopic healthy eyes. We then use these landmarks to define exposed neural canal and exposed scleral flange regions and report their prevalence and magnitude to be greatest within the inferior-temporal ONH Foveal-BMO sectors.

Taxonomy topics

Optic Nerve Head; Neural Canal; Glaucoma; 3D Imaging; Optical Coherence Tomography; Imaging Anatomy; Bruch' Membrane Opening; Anterior Scleral Canal Opening; Myopia; Scleral Flange; Dural Sheath; Scleral Flange Opening; Glaucoma; Myopia

INTRODUCTION

In axial myopia,[1] elongation of the eye is accompanied by structural changes to the choroid, sclera, retina and optic nerve head (ONH) tissues that contribute to the clinical appearance of myopic optic disc "tilt", "torsion" and "peripapillary" "atrophy".[2–7] While refractive error and axial length are commonly used to clinically define myopia and assess its progression,[8] until recently,[9–13] there have been no OCT parameterization strategies to detect, quantify

and stage the morphologic character of myopic structural alteration to the ONH neural and connective tissues that were based entirely on OCT-detected anatomic landmarks.

We define the ONH anatomically and morphologically (Figure 1) to include the tissues within the neural canal and those immediately adjacent to it.[13,14] These include, the perineural canal (pNC) retina, choroid, and sclera, the immediate retrolaminar orbital optic nerve, the dural and pial sheath insertions and the medial portion of the inferior oblique muscle insertion. (Supplemental Figure 1).[13] We have previously defined the neural canal to be the connective tissue pathway through the choroid and sclera through which the retinal ganglion cell (RGC) axons achieve the orbital optic nerve (Figures 2 and 3).[9,12,14–17] The pre-scleral neural canal (Figures 1 and 2) extends from Bruch's membrane opening, (BMO), to the anterior scleral canal opening, (ASCO). It consists of the connective tissue component of the choroidal border tissues (CBT) which are known histologically as the border tissues of Elschnig.[15,18,19] The scleral portion of the neural canal extends from the ASCO through the scleral flange opening, (when present - see Methods and Figure 1), ending at the posterior scleral canal opening which can be identified histologically[14,16,17,20] but is inconsistently visualized by OCT. In both monkey, (quantitatively)[14,16,17] and human (through qualitative inspection)[20–22] studies, the transverse size of the neural canal increases as it passes through the sclera. Correspondingly, there is a profound increase in the size of the retrobulbar nerve relative to the size of the "clinical optic disc" (Supplemental Figure 1).

In this report we use the term pNC to distinguish OCT ONH terminology, (which we argue should be based on OCT-detected anatomic landmarks) from the traditional term "optic disc" and derivative terms such as "peripapillary" because these terms, being based on the clinical disc margin, have no consistent OCT-detectable anatomic foundation in the human eye.[23,24] Having no consistent anatomic foundation, the clinical disc margin is inconsistently assigned by clinicians[25] leading to inaccuracy in their rim tissue assessment (Supplemental Figure 1).[24,26] Because the clinical disc margin is also used in the definitions of "optic disc tilt" and "torsion" as well as the clinical "gamma", "delta" and "peripapillary atrophy" zones, it has contributed to the lack of anatomically consistent OCT definitions for these terms.[4,27,28]

For this study we manually segmented the OCT-defined scleral flange opening (SFO), a new OCT ONH neural canal anatomic landmark, in non-highly myopic eyes and used it to define a new ONH region – the exposed neural canal (ENC) region. We define an ENC region to consist of two sub-regions, an externally oblique choroidal border tissue (EOCBT) region and/or an exposed scleral flange (ESF) region (Figures 2–4). In this nomenclature, we use the term "exposed" in two contexts. First, in the case of the ESF region, we hypothesize that the "anterior" scleral flange surface (Figures 5–6), once physically covered by retinal pigment epithelium (RPE), Bruch's membrane (BM) and choroid, is now clinically "exposed" due a shift of BM and BMO relative to the ASCO and subsequent CBT migration away from the SFO. Second in the case of the CBT and internal scleral flange surfaces (Figures 5–6), we hypothesize that tissues which were once internally oblique or vertical (axial) in orientation, (and thus less clinically visible), are now, through displacement, deformation or remodeling, more externally oblique, (i.e., more transverse

– Figures 1–2) in orientation and therefore more “exposed” to clinical observation. These hypotheses are more completely explained in the Discussion.

In previous post-mortem monkey studies,[14,16] we defined the scleral flange to be the portion of the pNC-sclera that was “internal” to the posterior scleral canal opening (PSCO). In separate studies in post-mortem human eyes,[29,30] Jonas defined the scleral flange to be the portion of the pNC-sclera that was “central “or “internal” to the dural sheath insertion (Figure 5). These independent definitions are complimentary because they suggest two independent mechanisms of scleral flange development that may be synergistic. First, scleral flange morphology is influenced by transverse neural canal enlargement within the sclera and second that it is influenced by the dural sheath addition of substantial thickness to the outer layers of the pNC-sclera, peripheral to the flange.[14,16] Multiple investigators[31–34] have hypothesized that the relative thinness and obliqueness of the scleral flange (without necessarily using that term) may have biomechanical implications on the loading of the lamina cribrosa (the primary site of injury to the RGC axon in glaucoma).

From the standpoint of ONH biomechanics and ONH blood flow,[31–33,35–38] in most human eyes, the pNC-scleral flange contains the juxta-canalicular collagen and elastin ring,[39–43] the vascular circle of Zinn-Haller,[44–47] as well as the penetrating branches of the posterior ciliary arteries.[44] It is thus likely that the scleral flange tissues are the primary site of the complicated interactions between the laminar beam insertions and the collagen and elastin ring that generate deformation and strain.[31,48–50] In addition, in most eyes, the pNC-scleral flange tissues likely directly experience the primary effects of eye-movement-induced fluctuations in dural sheath and dural sheath scleral insertion loading.[51–57] Taken together, these biomechanical effects are hypothesized to include diminished blood flow within the small posterior ciliary artery branches which pass through the scleral flange to supply the lamina cribrosa and juxta-canalicular choroid (the choroidal region most susceptible to clinical “peripapillary” atrophy).[31,36–38]

We propose that an OCT ENC region occurs when, through development or postdevelopmental “myopic” remodeling, BMO enlarges and/or becomes temporally displaced relative to the underlying ASCO and SFO (or, equivalently, the SFO and ASCO become nasally displaced relative to BMO). Because, the position of BMO relative to the ASCO and the SFO largely determines the character of an EOCBT or ESF region, (i.e., their sectoral location, extent and radial magnitude), in this study we report BMO offset relative to ASCO (BMO/ASCO offset), (see Methods). We additionally propose comprehensive OCT neural canal and scleral flange terminology (Table 1 and Supplemental Table 1), provide representative OCT examples of ENC regions and their appearance within non-highly myopic healthy study eyes and a representative highly myopic eye (Figures 3 and 4), and provide OCT depictions of ONH scleral flange anatomy in Figures 5 and 6.

In this study, we report the prevalence and character of the ENC region, (along with the EOCBT and ESF sub-regions), in 362 non-highly myopic healthy eyes of 362 subjects. We then test the hypothesis that the magnitude of an ESF sub-region in a given eye, inversely correlates with peri-neural canal (pNC) choroidal thickness (pNC-CT) within twelve 30° ONH sectors (Figure 2) assigned relative to the Foveal-BMO axis.

Methods

Definitions and Terminology (Table 1, Supplemental Table 1 and Figures 1–6).

OCT neural canal and scleral flange anatomic terminology (Table 1 and Supplemental 2) is explained and illustrated in Figures 1 – 6. While in previous reports[9,58] we referred to the CBT by their histologic name ("Border Tissues of Elschnig"), we now[13] refer to them as the CBT, only. All left eye data were converted to right eye configuration for analysis and presentation except as noted. Quantification of all parameters was performed with Matlab R2016a (Matlab version 9.0.0.341360; The MathWorks, Natick, MA).

Subjects.—A total of 362 healthy individuals were recruited from 8 centers (5 in the United States, 2 in Germany and 1 in Canada) as previously described.[59] Each participant provided signed informed consent. The study adhered to the declaration of Helsinki for research involving human subjects and was approved by the institutional review board of each participating institution.

OCT Image Acquisition and Segmentation.

The ONH, pNC- RNFL and macula were imaged with spectral domain OCT (Spectralis, Heidelberg Engineering GmbH, Heidelberg, Germany, software version Heyex 1.9.10.0). For each eye, prior to image acquisition, refractive correction and keratometry values were entered. The operator then manually identified and marked the fovea in a live B-scan, then centered the imaging field on the ONH, where the 2 BMO points in each of 2 perpendicular ONH radial B-scans were identified. These steps established the eye-specific, FoBMO axis, which was used as the reference for the acquisition of all OCT B-scans.[59–61] The complete ONH imaging pattern consisted of 24 radial B-scans (15° apart with each B-scan containing 768 A-scans) centered on BMO and acquired in Enhanced Depth Imaging mode[62] with an average of 25 repetitions each.

Our strategy for OCT ONH image manual segmentation has been described previously.[9,10,63,64] Segmented landmarks included: the internal limiting membrane (ILM); posterior surface of the RNFL, posterior surface of the Bruch's membrane/retinal pigment epithelium complex, BMO, neural canal wall, anterior scleral surface, and the ASCO (segmented on each side of the canal by visually projecting the plane of the peripapillary anterior scleral surface through the neural canal wall and marking their intersection).[9,10,63,64]

For the present study, the SFO was manually segmented by a single operator (SWH) using one of two techniques (Figure 5, Panels A2-C2). The SFO was "geometrically" segmented when the transition from the "anterior" to the "internal" surface of the scleral flange was acute enough to be visually identified (Figure 5 panels B2 and C2). When the transition was not acute enough to be identified visually, it was estimated by visually projecting the anterior laminar surface through the neural canal wall (Figure 5, Panel A2). In all instances, the operator was able to inspect adjacent B-scans on either side of the B-scan in question to inform their final SFO segmentation choice.

Sectoral ENC, EOCBT and ESF Measurements (Figures 5 and 6).—Segmented BMO, ASCO and SFO points along with the segmented BMO centroid were projected to the BMO reference plane (Figure 5, panels A4 - C4) for re-sampled measurement within 30° sectors (Figure 6A and 6B). BMO, ASCO and SFO B splines were then plotted within the BMO reference plane. Within each sector, four equally- spaced re-sampling lines were used to measure the radial extent (magnitude) of the EOCBT, ESF and ENC (the sum of the two) regions (Figure 6C). Data from these four measurements of each region were then averaged. Data from Sectors with less than 2 measurements were not included (i.e., the region was treated as not present (0 magnitude) in that sector. For a given eye, the definition for the presence of an EOCBT or ESF region (alone or together constituting an ENC region) – required the presence of that region in 2 contiguous FoBMO sectors.

While BMO demarcates the peripheral extent of the EOCBT in most sectors of most eyes, in those sectors in which BM extends beyond the CBT and BMO overhangs (i.e., is internal to) the CBT insertion into BM, (Supplemental Figure 2), the CBT BM insertion (CBT-BMI) was used to define the peripheral extent of the EOCBT region. However, because the length of BM overhangs, when present, were small, the use of CBT-BMI, when required, only minimally affected the EOCBT magnitude measurement.

BMO/ASCO Offset Magnitude and Direction (Supplemental Figure 3).—As previously described,[9,12] for each study eye, a plane was fitted to the 48 segmented BMO and ASCO points, respectively, by minimizing the mean squared axial error.[65] The BMO coordinates were projected to the BMO reference plane. Thereafter, a best-fit ellipse was fitted,[65] and the BMO and ASCO centroids and areas were calculated. BMO/ASCO offset magnitude and direction were defined by projecting the BMO/ASCO centroid vector (the vector connecting the ASCO and BMO centroids to the BMO reference plane and transposing the vector from the ASCO to the BMO for direction and offset magnitude quantification relative to the FoBMO axis. It is thus equal in magnitude but 180° opposite in direction to our previously reported parameter ASCO/BMO offset.[9,12]

BMO, ASCO, SFO/ASCO Conjugate Opening and Neural Canal Minimum Cross-Sectional Area (NCMCA) Size and Shape Measurements (Figure 8).

The size and shape (ovality index) of BMO and ASCO were assessed using a best-fit ellipse within their respective best fit reference planes. For the SFO/ASCO conjugate opening, the 48 SFO/ASCO conjugate opening points consisted of the SFO points where present, and the ASCO points at the radial locations where an SFO point was not present. SFO/ASCO conjugate opening size and shape was then assessed using a best-fit ellipse within the best fit reference plane. As previously defined,[9,12] NCMCA (Figure 8 and Supplemental Figure 4)[9] estimates the size and shape of the smallest opening through which the RGC axons must pass as they traverse the pre-scleral neural canal.

pNC Choroidal Thickness (pNC-CT).—Sectoral pNC-CT measurements were generated from the 24 radials B-scans as previously reported[10,13,64] and illustrated in Supplemental Figure 5. For each sector of each study eye, pNC-CT was expressed both in microns and as its age-corrected, normative range percentile.

Inter-observer reproducibility.—The effect of inter-observer SFO segmentation reproducibility was assessed for the parameters ESF length using the manual SFO segmentations of two independent operators (SWH and HY) from the same 20 OCT data sets. To do so, the two operators, independently marked the scleral flange opening (SFO) (when present) in the 48 radial OCT B scan images from the same 20 reproducibility study eyes while the existing ASCO segmentations were held constant within the data sets of both operators. ESF length for each sector was then calculated for each observer (using their own SFO and the common ASCO) for each sector of each reproducibility study eye.

Statistical Analysis.

All statistical analyses were performed with R Studio (version 2022.12.0+353 - The R Foundation for Statistical Computing, Vienna, Austria) or SPSS (IBM SPSS, Inc.). Descriptive statistics included the mean and standard deviation for continuous variables and proportions for categorical variables. The T-test (continuous variable) or Chi-square test (dichotomous variable) were used to compare characteristics between groups. Intra-class correlation coefficients (ICC) between observers for ESF length were calculated using a two-way mixed model for agreement. Ocular and demographic effects on the OCT ENC, EOCBT and the ESF regions were assessed using univariable and multivariable linear regression, ensuring the variance inflation factor remained below 5 to avoid excessive multicollinearity.

Within the Non-Hi-ESF and Hi-ESF study eyes the correlations between the sectoral magnitude of the ESF and the proportional pNC-CT were separately assessed for each group at the 100, 300, 700 and 1100 μm pNC-CT measurement points using a generalized estimation equation linear model. Prior to this analysis, instead of using the raw measurement values, a natural log transformation was applied to the pNC-CT data, (i.e., they were converted to log (raw value) to ensure the residuals of the model were normally distributed (i.e., were more Gaussian). Log transformed pNC-CT raw data was then converted to proportional thickness relative to the log transformed normative data base sectoral average, (log(raw value) / log(normal value for that sector)) so as to eliminate the effects of the known (i.e., well established) sectoral variation in pNC-CT.

Correlations between the SFO/ASCO Conjugate Opening and NCMCA, between the SFO/ASCO Conjugate Opening and RNFLT (3.5 and 4.1mm) and between NCMCA and RNFLT (3.5 and 4.1mm) were performed using simple linear regression. For these correlations, in the 183 eyes in which the ESF region magnitude was > 0 the SFO/ASCO Conjugate Opening was defined by the SFO and ASCO points. In the 179 eyes without an ESF region the SFO/ASCO conjugate opening was defined by the ASCO points.

Multiple Comparisons.—For all analyses, we report comparisons with $p < 0.05$ as significant but emphasize those that achieved significance using our most stringent criteria for type I error correction (Holm-Bonferroni).[66]

Results

Study Subjects and Eyes.

Three hundred sixty-two non-highly myopic eyes of 362 subjects were studied. Demographic and ocular data are reported in Table 2.

Inter-observer SFO Reproducibility.

Segmentation reproducibility for all OCT anatomic landmarks of this report, except the SFO, have been previously reported.[9,10,59,63,64] ICC values for ESF region length for all 12 sectors ranged from 0.928–0.996. However, because only 3 (15%) reproducibility study eyes had ESF regions in the superior nasal (SN) sector, the p values for the ICC values for that sector were lower (see Supplemental Table 2).

Subdivision of Study eyes into Hi-ESF and Non-Hi-ESF subgroups.

To test the hypothesis that non-highly myopic eyes with the largest ESF regions represented a form of neural canal remodeling that would have distinguishable features, we defined Hi-ESF eyes to be those that contained at least one FoBMO sector with an ESF region > 100 μms in length. We then compared the n=73 Hi-ESF study eyes (20.5% of all study eyes by this definition) to the 289 Non-Hi-ESF study eyes in a series of subsequent analyses (Table 3).

Ocular and demographic differences between Hi-ESF and Non-Hi-ESF eyes.

Hi-ESF eyes demonstrated significantly longer axial length, greater myopic spherical equivalent, larger BMO area, increased BMO/ASCO area ratio, decreased NCMCA, increased BMO/ASCO offset magnitude, and decreased proportional pNC-CT at all measurement points with the differences achieving significance at the pNC-CT-1100 measurement point (Table 2). The mean length of the ENC EOCBT and ESF regions was profoundly increased in the Hi-ESF versus the Non-Hi-ESF eyes (Table 3).

The sectoral prevalence of the ENC region and EOCBT and ESF subregions was greatest in the inferior temporal sectors.—The highest sectoral prevalence of each region or sub-region (ENC 40.9%; EOCBT 39.8%; ESF 34%; and Hi-ESF 18.2%) occurred within the inferior-temporal or temporal-inferior sectors (Figure 9).

The maximum ENC, EOCBT and ESF lengths in the Hi-ESF eyes occurred within the inferior temporal sectors where the adjacent pNC-CT was thinnest at all four pNC-CT measurement points.—Figure 10 reports sectoral mean ENC, EOCBT and ESF lengths as well as mean sectoral pNC-CT (300) thickness within All Study eyes (upper row), the Non-Hi-ESF eyes (middle row) and the Hi-ESF eyes (lower row). Supplemental Figure 6 reports mean pNC-CT data at all four pNC-CT measurement points. These data strongly suggest that in the Hi-ESF eyes, the ENC regions were longest and the pNC-CT was thinnest within the inferior temporal sectors. Supplemental Figure 7 separately demonstrates that the magnitude of sectoral ESF is inversely correlated with the natural log proportional pNC-CT at the 100 μm (R^2=0.16, $p < 0.0001$) measurement point. Correlations

at the pNC-CT- 300 μm (R^2=0.12), 700 μm (R^2=0.13), and 1100 μm (R^2=0.14) measurement points were also significant.

BMO/ASCO offset was increased in the Hi-ESF eyes.

BMO/ASCO offset was more than 2x greater, on average, within the Hi-ESF eyes (Table 2). The greatest frequency and magnitude of BMO/ASCO offset occurred within the inferior-temporal quadrant and the largest BMO/ASCO offset occurred almost exclusively in the Hi-ESF eyes. (Figure 11).

BMO,ASCO, SFO/ASCO Conjugate Opening, and NCMCA Size and Shape.— While the size of BMO (Supplemental Figure 8 and Table 4) was significantly increased in the Hi-ESF compared to the Non-Hi-ESF eyes, the shape of BMO was not different, nor was the size and shape of the ASCO different between the two groups. However, both the SFO/ASCO Conjugate Opening (moderately) and the NCMCA (substantially) were decreased in size and more oval in shape in the Hi-ESF compared to the Non-Hi-ESF eyes. Supplemental Table 3 reports univariable and multivariable associations with the ENC region and sub-regions in the 73 Hi-ESF eyes. Supplemental Table 4 reports the same associations within the 183 study eyes demonstrating an ENC regions. Within both analyses, the strongest associations were with BMO/ASCO area ratio and BMO/ASCO offset magnitude.

Correlations among SFO/ASCO Conjugate Opening Area, NCMCA and Global RNFLT.

Within the data from all study eyes, SFO/ASCO Conjugate Opening Area significantly correlated with NCMCA (R^2=0.3175, P<0.0001) and Global RNFLT (3.5/4.1 mm) (R^2=0.12/0.13, P<0.0001). The correlation between NCMCA and RNFLT (3.5/4.1mm) (R^2=0.14/0.15, P<0.0001) was also significant (Supplemental Figure 9).

Discussion

Since Helmholtz introduced the direct ophthalmoscope in 1851,[67] and through the later implementation of slit lamp biomicroscopy and fundus photography, the clinical evaluation of the ONH tissues has been limited to what clinicians can see on its surface. Thirty years after the introduction of OCT imaging,[68] clinicians still struggle to integrate deep OCT ONH anatomy and morphology into their clinical examination of the ONH tissues. To date, there have been no attempts to parameterize the scleral flange using OCT-detected anatomic landmarks. While the clinical “gamma” and “delta” “parapapillary” “atrophy” zones are sometimes suggested to be surrogate measures of the scleral flange, because they are defined based on the clinical disc margin, these regions do not have a consistent anatomic foundation, and have therefore never been consistently defined using OCT.[4,27,28]

Our study introduces the SFO as a new deep neural canal anatomic landmark, proposes a conceptual framework for understanding its importance, and is the first to manually segment it using OCT. It then uses the OCT-defined SFO, BMO and the ASCO to introduce the ONH ENC region, defining it to be exposed neural canal wall, (not atrophy),[4,27,28] and therefore “within” the neural canal (not peri-neural canal and thus not *“peripapillary”*). Our study further defines the ENC region to consist of EOCBT and/or ESF subregions,

articulates OCT-based anatomic concepts and terminology to characterize the ONH tissues relative to the neural canal instead of the clinical disc margin and introduces terminology for characterizing neural canal scleral flange remodeling using OCT. Finally, our approach allowed us to identify 73 non-highly myopic eyes demonstrating a “Hi-ESF” region and characterize their ONH morphologic differences from the 289 “Non-Hi-ESF” study eyes.

Among all study eyes, but especially among the Hi-ESF eyes, the ESF region occurred most frequently and was greatest in magnitude within the inferior temporal sectors, where BMO/ASCO offset also was also greatest in prevalence and magnitude and pNC-CT was proportionally thinnest. These findings complement our previous report that pNC scleral bowing (pNC-SB) was greatest within the inferior temporal sectors of the same non-highly myopic eyes of this study.[10] They additionally complement the findings of our recent report on pNC-SB and pNC-CT within a separate group of highly myopic eyes.[13]

We propose that BMO-ASCO offset[9,12] and pNC-SB[10,13] are core mechanistic components and/or important secondary manifestations of myopic ONH remodeling that can be present in eyes with all levels of refractive and axial myopia. We therefore predict that the sectoral location and magnitude of pNC-SB will correlate with the sectoral location and magnitude of the ENC region in non-highly myopic and highly myopic eyes. While beyond the scope of the present report, the relationships between and among the ESF region, BMO/ASCO offset, pNC-SB, pNC-CT and pNC-RNFLT, (all characterized relative to the FoBMO axis) are under study in an expanded group of non-highly myopic and highly myopic eyes that will be the subject of a follow up report.

The fact that Hi-ESF eye increases in BMO/ASCO offset and proportional decreases in pNC-CT were greatest within the inferior temporal sectors, and that within individual Hi-ESF eyes the choroid is proportionally thinnest (i.e., the lowest normative percentile values will occur) within the highest ESF sectors, is important because a large literature in non-highly myopic eyes has shown these sectors to be most susceptible to the structural alterations of aging and glaucoma.[69–74] While the mechanisms of this inferior temporal ONH susceptibility remain unknown, we hypothesize that the biomechanical links between the pNC-sclera, the dural sheath insertion, the laminar beam insertions and the scleral flange, outlined in the introduction, may effect blood flow through the small penetrating branches of the posterior ciliary arteries that pass through these tissues to supply the circle of Zinn-Haller, the pNC-choroid and the laminar beams.[44,45,47] Hayreh demonstrated this blood supply to be preferentially susceptible to acute IOP elevation in monkeys,[37] and hypothesized that its compromise contributed to a vascular insult in glaucoma and the frequent presence of pNC choroidal atrophy in aging and glaucoma.[37,75] Longitudinal studies to assess whether the location and magnitude of an ENC region predicts such susceptibility are necessary and can now be consistently performed using the OCT parameters and techniques described herein.

Additional Implications, Predictions and Clarifications.

In Figure 12, we propose that the primary posterior scleral, scleral flange, choroidal and retinal remodeling of axial myopia together cause or are accompanied by primary and secondary optic nerve head (ONH) neural canal remodeling processes that can be

highly variable among and between eyes. The existing ENC region from the 48-year-old highly myopic example eye from Figures 3–6 is used to create a “Proposed Longitudinal Change” scenario (Far-Left and Left-Middle Panels) in which choroidal border tissue (CBT) “externalization” and “insertion migration” away from the original anterior scleral canal opening (ASCO) leaves an ESF region and a geometrically identifiable SFO. Taken together, these panels suggest that in the setting of CBT migration away from the SFO, the SFO is synonymous with the ASCO at the end of development (i.e., prior to the onset of myopic neural canal remodeling).

However, an “Alternative Longitudinal Change” scenario (Figure 12, Right-Middle and Far-Right Panels) can be imagined, (based on the appearance of other highly myopic eyes (manuscript in preparation)), in which the CBT is externalized and elongates progressively without losing its insertion into the original ASCO (Far-Right Panel). Had this CBT remodeling scenario occurred, the expected composition of the ENC region would consist entirely of an EOCBT region only – without creating an ESF region.

In both of the above scenarios, it must be acknowledged that some ESF regions may have intact CBT present that is in physical apposition to or has become optically indistinguishable from the underlying anterior scleral flange surface due to choroidal atrophy. In these eyes, our concept of CBT “insertion migration” would be replaced by choroidal atrophy and CBT/anterior scleral apposition. However, our concept that the SFO is the original ASCO would not change.

Our hypothesis that the SFO (and therefore the entire SFO/BMO conjugate opening) represents the ASCO at the end of embryologic (i.e., pre-myopic) development has the following implication. First, the fact that the SFOF/ASCO conjugate opening is smaller and slightly more oval in the Hi-ESF compared to the Non-Hi-ESF suggests that eyes demonstrating a high ESF region may have undergone a contraction of the postdevelopmental ASCO opening that is greater horizontally than vertically. However, it is also possible that the “apparent” contraction and ovalization of the SFO/ASCO conjugate opening is not due to a contraction in the size of its circumference but instead is due to a focal or symmetric “bending” or “warping” of the opening. Such a *“warped”* opening might appear to be smaller and more oval when projected to its “post-warped” reference plane. Future longitudinal studies are required to confirm the character of SFO/ASCO conjugate opening remodeling through the full spectrum of ONH myopic structural alteration.

A series of longitudinal studies directly or indirectly provide evidence in support of the hypotheses illustrated in Figure 12. Kim and coauthors,[76] schematically suggested a temporal shift of BMO relative to the underlying ASCO as the cause of the appearance of a “temporal crescent” in longitudinal color photographs of a young child with myopia. While employing standard nomenclature at the time, they incorrectly identified the crescent as “parapapillary”, (see Introduction), but correctly suggested that the crescent “was formerly an inner surface of the scleral canal”.

In a series of important publications,[77,78] the Boramae Myopia Cohort Study has used longitudinal OCT imaging in children with progressive myopia to describe longitudinal

increases in the temporal crescent of clinical “peripapillary atrophy”. While the images in their reports qualitatively include OCT detected EOCBT elongation and or progressive ESF increases, this terminology has not been used nor has the SFO been segmented. Finally, Kim and colleagues,[79] used swept source OCT to describe longitudinal changes in the CBT that are compatible with the migration and elongation proposed in Figure 12. However, the SFO and ASCO were not segmented and BMO enlargement was emphasized as the underlying mechanism. While a temporal shift of BMO relative to the underlying ASCO is suggested in several figures, this phenomenon was not commented upon.

In Figure 13, longitudinal OCT imaging from a previously reported[80] mildly myopic eye (−1.50 D SE at baseline and −3.0 D SE at follow up) demonstrates inferior-temporal expansion of an ENC region that includes CBT insertion migration, CBT extension and the suggestion of neural canal contraction and shape change. In these images, because Heidelberg Engineering Spectralis OCT Baseline and Follow Up images are acquired using eye-tracking software[81] relative to the arcuate retinal vasculature, (rather than the ONH vasculature), the position of the center of radial B-scan acquisition (red-dotted cross-hairs) is held stable relative to the retinal vessels, isolating the movement of the deep ONH anatomy relative to the retinal vessels (and thus relative to BMO). Note that the clinical “shadow” of the neural canal appears smaller, more oval in shape and is superior-nasally displaced in the “Follow Up” infrared images. Note also that the ASCO and SFO segmented points are shifted superior nasally, contracted and ovalized in the Follow Up (compared to the Baseline) images. Finally, while BMO does not appear to be profoundly altered in size or position within the Follow Up image, the ASCO and SFO appear smaller and shifted nasally relative to BMO.

Finally, while the prevalence and magnitude of BMO/ASCO offset increases with axial length in non-highly myopic[9] and highly myopic eyes,[12] substantial ENC regions were present in a small subset of hyperopic eyes (Supplemental Figure 10). The clinical implications of the ENC region in hyperopic eyes remains to be determined.

Limitations.

In this paper (and those that precede it),[63,64] we identified the ASCO by projecting the immediate pNC anterior scleral surface through the CBT to the neural canal wall (Figures 1–6). Unlike BMO, which is an anatomically identifiable structure in most non-highly myopic eyes by histology and by OCT,[15,82–84] the ASCO is not an anatomically identifiable structure in either modality. However, although ASCO was estimated in the described manner, the inter-operator reproducibility of ASCO area and all related parameters was excellent in a previous study in which it was assessed in these same study eyes.[63]

Unlike, the ASCO, we believe that the SFO is an anatomically identifiable opening in most sectors of most eyes in which it appears. This is especially true for eyes in which the maximum length of the flange equals or exceeds 100 microns as in the Hi-ESF eyes of this study. However, scleral flange remodeling can include a highly variable combination of primary scleral flange shape change as well as fusion of the pial sheath, scleral flange and laminar beam insertions[27] which together can make the SFO location challenging to identify.

Acknowledging these challenges, in this study the reproducibility of SFO identification by two independent operators was excellent (see Supplemental Table 2).

An important finding of this study is that “myopic” neural canal remodeling, (as defined by the presence of a High-ESF region) was present in approximately 20% of non-highly myopic healthy eyes. These included eyes that demonstrated hyperopic refractive errors and moderate axial lengths (Supplemental Figure 10). Of these, 3 eyes demonstrated axial lengths greater than 26.00 mm (FDA299 (26.07 mm); FDA319 (26.44 mm); and FDA266 (26.44 mm)), a definition of high myopia in some studies.[85]

Finally, the integration of our OCT landmarks and parameters into clinical practice will be delayed by the need for manual segmentation of our anatomic targets. However, within ongoing collaborations with several laboratories we are using the segmentations from the eyes in this report as well as those from a previously published group of highly myopic eyes,[12,13] (manuscript in preparation), to build automated segmentation algorithms to aid this transition. In these regards, an additional group of 1080 eyes will be available to us and others as a product of the Glaucoma/Myopia OCT Phenotyping Consortium which has just begun subject recruitment (www.gmopconsortium.org).[13]

Summary.

Our study defines a new ONH neural canal anatomic landmark, the SFO, and enables its incorporation, along with the ESF and ENC regions it defines, into OCT strategies to structurally stage the optic neuropathies of aging, glaucoma and myopia in the human eye. In a manuscript in preparation, we will expand our characterization of the ENC, EOCBT and ESF regions into highly myopic eyes.[12,13] In so doing, we will lay the foundation for future longitudinal studies that will characterize the development and clinical implications of ENC Hi-ESF regions in non-highly myopic and highly myopic eyes.

Supplementary Material

Refer to Web version on PubMed Central for supplementary material.

Acknowledgements/Disclosure

Funding/ Support:

NIH/NEI R01-EY021281; Legacy Good Samaritan Foundation; Heidelberg Engineering, GmbH, Heidelberg, Germany.

Financial Disclosure:

SW. Hong: None. H. Yang: None. S. Gardiner: Nonfinancial support – Heidelberg Engineering. G. Sharpe: None. J. Caprioli: None. S. Demirel: None. C. A. Girkin: Financial support - Heidelberg Engineering. C. Y. Mardin; Financial support - Heidelberg Engineering. H. A. Quigley: Financial support - Heidelberg Engineering. A. F. Scheuerle: Financial support - Heidelberg Engineering. A. Jiravarnsirikul: None. B. Fortune: Financial support - Legacy Good Samaritan Foundation, Inotek Pharmaceuticals. B.C. Chauhan: Financial support - Heidelberg Engineering. C. F. Burgoyne: Financial support - NIH/NEI R01-EY021281, Legacy Good Samaritan Foundation, Heidelberg Engineering.

* The above listed sponsors/funding organizations had no role in the design, conduct, analysis or reporting of this research.

Other Acknowledgments

Drs Seungwoo Hong and Hongli Yang contributed equally to this work.

Abbreviations/Acronyms (see Table 1):

ASCO	anterior sclera canal opening
BM	Bruch's Membrane
BMO	Bruch's membrane opening
CBT	Choroidal Border Tissues – previously referred to by their histologic name ("Border tissues of Elschnig")
CCT	central corneal thickness
CDM	clinical disc margin
ENC	Exposed Neural Canal
EOCBT	Externally Oblique CBT
ESF	Exposed Scleral Flange
FDA	Food and Drug Administration
FoBMO	Foveal-BMO
Hi-ESF	Study Eyes in which the ESF region is ≥ 100 μms in at least one sector
IOCBT	Internally Oblique Choroidal Border Tissues
NC	Neural Canal
NCMCA	Neural Canal Minimum Cross-Sectional Area
Non-Hi-ESF	Study eyes in which the ESF region is < 100 μms in all sectors
PSCO	Posterior Scleral Canal Opening (Not segmented in this study)
OCT	optical coherence tomography
ONH	optic nerve head
pNC	perineural canal
pNC-CT	perineural canal choroidal thickness
RNFL	retinal nerve fiber layer
RNFLT	RNFL thickness

RPE	Retinal Pigment Epithelium
Sector	ONH FoBMO 30° (clock-hour) sectors (see Figure 2, Panel (A))
SFO	Scleral Flange Opening
SD	standard deviation
SE	spherical equivalent

References

1. Flitcroft DI, He M, Jonas JB, et al. IMI - Defining and Classifying Myopia: A Proposed Set of Standards for Clinical and Epidemiologic Studies. IOVS. Feb 28 2019;60(3):M20–M30. doi:10.1167/iovs.18-25957
2. Hwang YH, Yoo C, Kim YY. Characteristics of peripapillary retinal nerve fiber layer thickness in eyes with myopic optic disc tilt and rotation. J Glaucoma. Aug 2012;21(6):394–400. doi:10.1097/IJG.0b013e3182182567 [PubMed: 21946540]
3. Hwang YH, Yoo C, Kim YY. Myopic optic disc tilt and the characteristics of peripapillary retinal nerve fiber layer thickness measured by spectral-domain optical coherence tomography. J Glaucoma. Apr-May 2012;21(4):260–5. doi:10.1097/IJG.0b013e31820719e1 [PubMed: 21623226]
4. Park HY, Choi SI, Choi JA, Park CK. Disc Torsion and Vertical Disc Tilt Are Related to Subfoveal Scleral Thickness in Open-Angle Glaucoma Patients With Myopia. IOVS. Jul 2015;56(8):4927–35. doi:10.1167/iovs.14-15819
5. Yamashita T, Sakamoto T, Yoshihara N, et al. Circumpapillary course of retinal pigment epithelium can be fit to sine wave and amplitude of sine wave is significantly correlated with ovality ratio of optic disc. PLoS One. 2015;10(4):e0122191. doi:10.1371/journal.pone.0122191 [PubMed: 25848777]
6. Shoji T, Kuroda H, Suzuki M, Ibuki H, Araie M, Yoneya S. Vertical asymmetry of lamina cribrosa tilt angles using wide bandwidth, femtosecond mode-locked laser OCT; effect of myopia and glaucoma. Graefes Arch Clin Exp Ophthalmol. Jan 2017;255(1):197–205. doi:10.1007/s00417-016-3524-6 [PubMed: 27796669]
7. Shoji T, Kuroda H, Suzuki M, et al. Correlation between Lamina Cribrosa Tilt Angles, Myopia and Glaucoma Using OCT with a Wide Bandwidth Femtosecond Mode-Locked Laser. PLOS ONE. 2015;9(12):e116305. doi:10.1371/journal.pone.0116305
8. Holden BA, Fricke TR, Wilson DA, et al. Global Prevalence of Myopia and High Myopia and Temporal Trends from 2000 through 2050. Ophthalmology. May 2016;123(5):1036–42. doi:10.1016/j.ophtha.2016.01.006 [PubMed: 26875007]
9. Hong S, Yang H, Gardiner SK, et al. OCT-Detected Optic Nerve Head Neural Canal Direction, Obliqueness, and Minimum Cross-Sectional Area in Healthy Eyes. AJO. Dec 2019;208:185–205. doi:10.1016/j.ajo.2019.05.009
10. Wang YX, Yang H, Luo H, et al. Peripapillary Scleral Bowing Increases with Age and Is Inversely Associated with Peripapillary Choroidal Thickness in Healthy Eyes. AJO. Sep 2020;217:91–103. doi:10.1016/j.ajo.2020.03.050
11. Tun TA, Wang X, Baskaran M, et al. Variation of Peripapillary Scleral Shape With Age. IOVS. Aug 1 2019;60(10):3275–3282. doi:10.1167/iovs.19-26777
12. Jeoung JW, Yang H, Gardiner S, et al. Optical Coherence Tomography Optic Nerve Head Morphology in Myopia I: Implications of Anterior Scleral Canal Opening Versus Bruch Membrane Opening Offset. AJO. Oct 2020;218:105–119. doi:10.1016/j.ajo.2020.05.015
13. Burgoyne CF, Wang YX, Jeoung JW, et al. OCT Optic Nerve Head Morphology in Myopia II: Peri-Neural Canal Scleral Bowing and Choroidal Thickness in High Myopia - An American Ophthalmological Society Thesis. AJO. Mar 9 2023;doi:10.1016/j.ajo.2023.03.002

14. Downs JC, Yang H, Girkin C, et al. Three-dimensional histomorphometry of the normal and early glaucomatous monkey optic nerve head: neural canal and subarachnoid space architecture. IOVS. Jul 2007;48(7):3195–208. doi:10.1167/iovs.07-0021
15. Strouthidis NG, Grimm J, Williams GA, Cull GA, Wilson DJ, Burgoyne CF. A comparison of optic nerve head morphology viewed by spectral domain optical coherence tomography and by serial histology. IOVS. Mar 2010;51(3):1464–74. doi:10.1167/iovs.09-3984
16. Yang H, Downs JC, Girkin C, et al. 3-D histomorphometry of the normal and early glaucomatous monkey optic nerve head: lamina cribrosa and peripapillary scleral position and thickness. IOVS. Oct 2007;48(10):4597–607. doi:10.1167/iovs.07-0349
17. Burgoyne CF, Downs JC, Bellezza AJ, Hart RT. Three-dimensional reconstruction of normal and early glaucoma monkey optic nerve head connective tissues. IOVS. Dec 2004;45(12):4388–99. doi:10.1167/iovs.04-0022
18. Anderson DR, Hoyt WF. Ultrastructure of intraorbital portion of human and monkey optic nerve. Arch Ophthalmol. Oct 1969;82(4):506–30. [PubMed: 4981187]
19. Hogan JJ, Alvarado JA, Weddell JE. Chapter 10 - Optic Nerve (Histology of the Human Eye). Histology of the Human Eye. WB Saunders Co.; 1971:523–606.
20. Girkin CA, Fazio MA, Yang H, et al. Variation in the Three-Dimensional Histomorphometry of the Normal Human Optic Nerve Head With Age and Race: Lamina Cribrosa and Peripapillary Scleral Thickness and Position. IOVS. Jul 01 2017;58(9):3759–3769. doi:10.1167/iovs.17-21842
21. Wilczek M The Lamina Cribrosa and its Nature. BJO. 1947;31(9):551–565.
22. Sigal IA, Flanagan JG, Tertinegg I, Ethier CR. 3D morphometry of the human optic nerve head. Exp Eye Res. Jan 2010;90(1):70–80. doi:10.1016/j.exer.2009.09.013 [PubMed: 19772858]
23. Reis AS, Sharpe GP, Yang H, Nicolela MT, Burgoyne CF, Chauhan BC. Optic disc margin anatomy in patients with glaucoma and normal controls with spectral domain optical coherence tomography. Ophthalmology. Apr 2012;119(4):738–47. doi:10.1016/j.ophtha.2011.09.054 [PubMed: 22222150]
24. Reis AS, O'Leary N, Yang H, et al. Influence of clinically invisible, but optical coherence tomography detected, optic disc margin anatomy on neuroretinal rim evaluation. IOVS. Apr 18 2012;53(4):1852–60. doi:10.1167/iovs.11-9309
25. Hong SW, Koenigsman H, Ren R, et al. Glaucoma Specialist Optic Disc Margin, Rim Margin, and Rim Width Discordance in Glaucoma and Glaucoma Suspect Eyes. AJO. Aug 2018;192(65–76):65–76. doi:10.1016/j.ajo.2018.04.022
26. Hong SW, Koenigsman H, Yang H, et al. Glaucoma Specialist Detection of Optical Coherence Tomography Suspicious Rim Tissue in Glaucoma and Glaucoma Suspect Eyes. AJO. Mar 2019;199:28–43. doi:10.1016/j.ajo.2018.10.027
27. Wang YX, Panda-Jonas S, Jonas JB. Optic nerve head anatomy in myopia and glaucoma, including parapapillary zones alpha, beta, gamma and delta: Histology and clinical features. Prog Retin Eye Res. Jul 2021;83:100933. doi:10.1016/j.preteyeres.2020.100933 [PubMed: 33309588]
28. Xue CC, Wang X, Han YX, et al. Parapapillary gamma zone associated with increased peripapillary scleral bowing: the Beijing Eye Study 2011. BJO. Sep 6 2022;doi:10.1136/bjo-2022-321868
29. Jonas JB, Jonas SB, Jonas RA, Holbach L, Panda-Jonas S. Histology of the parapapillary region in high myopia. AJO. Dec 2011;152(6):1021–9. doi:10.1016/j.ajo.2011.05.006
30. Vurgese S, Panda-Jonas S, Jonas JB. Scleral thickness in human eyes. PLoS One. 2012;7(1):e29692. doi:10.1371/journal.pone.0029692 [PubMed: 22238635]
31. Burgoyne CF, Downs JC, Bellezza AJ, Suh JK, Hart RT. The optic nerve head as a biomechanical structure: a new paradigm for understanding the role of IOP-related stress and strain in the pathophysiology of glaucomatous optic nerve head damage. Prog Retin Eye Res. Jan 2005;24(1):39–73. doi:10.1016/j.preteyeres.2004.06.001 [PubMed: 15555526]
32. Sigal IA, Flanagan JG, Tertinegg I, Ethier CR. Modeling individual-specific human optic nerve head biomechanics. Part I: IOP-induced deformations and influence of geometry. Biomech Model Mechanobiol. Apr 2009;8(2):85–98. doi:10.1007/s10237-008-0120-7 [PubMed: 18309526]

33. Burgoyne CF. A biomechanical paradigm for axonal insult within the optic nerve head in aging and glaucoma. Exp Eye Res. Aug 2011;93(2):120–32. doi:10.1016/j.exer.2010.09.005 [PubMed: 20849846]
34. Wang YX, Panda-Jonas S, Jonas JB. Optic nerve head anatomy in myopia and glaucoma, including parapapillary zones alpha, beta, gamma and delta: Histology and clinical features. Prog Retin Eye Res. Dec 9 2020:100933. doi:10.1016/j.preteyeres.2020.100933 [PubMed: 33309588]
35. Sigal IA, Flanagan JG, Tertinegg I, Ethier CR. Modeling individual-specific human optic nerve head biomechanics. Part II: influence of material properties. Biomech Model Mechanobiol. Apr 2009;8(2):99–109. doi:10.1007/s10237-008-0119-0 [PubMed: 18301933]
36. Burgoyne CF, Downs JC. Premise and prediction-how optic nerve head biomechanics underlies the susceptibility and clinical behavior of the aged optic nerve head. J Glaucoma. Jun-Jul 2008;17(4):318–28. doi:10.1097/IJG.0b013e31815a343b [PubMed: 18552618]
37. Hayreh SS. Pathogenesis of visual field defects. Role of the ciliary circulation. BJO. May 1970;54(5):289–311.
38. Hayreh SS, Revie IH, Edwards J. Vasogenic origin of visual field defects and optic nerve changes in glaucoma. BJO. Jul 1970;54(7):461–72.
39. Jan NJ, Lathrop K, Sigal IA. Collagen Architecture of the Posterior Pole: High-Resolution Wide Field of View Visualization and Analysis Using Polarized Light Microscopy. IOVS. Feb 01 2017;58(2):735–744. doi:10.1167/iovs.16-20772
40. Pijanka JK, Coudrillier B, Ziegler K, et al. Quantitative mapping of collagen fiber orientation in non-glaucoma and glaucoma posterior human sclerae. IOVS. Aug 2012;53(9):5258–70. doi:10.1167/iovs.12-9705 iovs.12–9705 [pii]
41. Downs JC, Blidner RA, Bellezza AJ, Thompson HW, Hart RT, Burgoyne CF. Peripapillary scleral thickness in perfusion-fixed normal monkey eyes. IOVS. Jul 2002;43(7):2229–35.
42. Quigley HA, Brown A, Dorman-Pease ME. Alterations in elastin of the optic nerve head in human and experimental glaucoma. BJO. Sep 1991;75(9):552–7.
43. Hernandez MR, Luo XX, Igoe F, Neufeld AH. Extracellular matrix of the human lamina cribrosa. AJO. Dec 15 1987;104(6):567–76.
44. Onda E, Cioffi GA, Bacon DR, Van Buskirk EM. Microvasculature of the human optic nerve. AJO. Jul 1995;120(1):92–102.
45. Jonas JB, Holbach L, Panda-Jonas S. Peripapillary arterial circle of Zinn-Haller: location and spatial relationships with myopia. PLoS One. 2013;8(11):e78867. doi:10.1371/journal.pone.0078867 [PubMed: 24223862]
46. Ohno-Matsui K, Kasahara K, Moriyama M. Detection of Zinn-Haller arterial ring in highly myopic eyes by simultaneous indocyanine green angiography and optical coherence tomography. AJO. May 2013;155(5):920–6. doi:10.1016/j.ajo.2012.12.010
47. Ishida T, Jonas JB, Ishii M, Shinohara K, Ikegaya Y, Ohno-Matsui K. Peripapillary Arterial Ring of Zinn-Haller in Highly Myopic Eyes as Detected by Optical Coherence Tomography Angiography. Retina. Feb 2017;37(2):299–304. doi:10.1097/IAE.0000000000001165 [PubMed: 27429391]
48. Bellezza AJ, Rintalan CJ, Thompson HW, Downs JC, Hart RT, Burgoyne CF. Anterior scleral canal geometry in pressurised (IOP 10) and non-pressurised (IOP 0) normal monkey eyes. BJO. Oct 2003;87(10):1284–90.
49. Sigal IA, Flanagan JG, Ethier CR. Factors influencing optic nerve head biomechanics. Invest Ophthalmol Vis Sci. Nov 2005;46(11):4189–99. [PubMed: 16249498]
50. Sigal IA, Flanagan JG, Tertinegg I, Ethier CR. Finite element modeling of optic nerve head biomechanics. Invest Ophthalmol Vis Sci. Dec 2004;45(12):4378–87. [PubMed: 15557446]
51. Chang MY, Shin A, Park J, et al. Deformation of Optic Nerve Head and Peripapillary Tissues by Horizontal Duction. AJO. Feb 2017;174:85–94. doi:10.1016/j.ajo.2016.10.001
52. Suh SY, Le A, Shin A, Park J, Demer JL. Progressive Deformation of the Optic Nerve Head and Peripapillary Structures by Graded Horizontal Duction. IOVS. Oct 1 2017;58(12):5015–5021. doi:10.1167/iovs.17-22596
53. Chen JY, Le A, De Andrade LM, Goseki T, Demer JL. Compression of the Choroid by Horizontal Duction. IOVS. Oct 1 2019;60(13):4285–4291. doi:10.1167/iovs.19-27522

54. Le A, Chen J, Lesgart M, Gawargious BA, Suh SY, Demer JL. Age-dependent Deformation of the Optic Nerve Head and Peripapillary Retina by Horizontal Duction. AJO. Jan 2020;209:107–116. doi:10.1016/j.ajo.2019.08.017
55. Wang X, Fisher LK, Milea D, Jonas JB, Girard MJ. Predictions of Optic Nerve Traction Forces and Peripapillary Tissue Stresses Following Horizontal Eye Movements. IOVS. Apr 1 2017;58(4):2044–2053. doi:10.1167/iovs.16-21319
56. Wang X, Rumpel H, Lim WE, et al. Finite Element Analysis Predicts Large Optic Nerve Head Strains During Horizontal Eye Movements. IOVS. May 1 2016;57(6):2452–62. doi:10.1167/iovs.15-18986
57. Wang X, Beotra MR, Tun TA, et al. In Vivo 3-Dimensional Strain Mapping Confirms Large Optic Nerve Head Deformations Following Horizontal Eye Movements. IOVS. Oct 1 2016;57(13):5825–5833. doi:10.1167/iovs.16-20560
58. Jeoung JW, Yang H, Gardiner SK, et al. DUPLICATE ENTRY SEE EN 9668 OCT Optic Nerve Head Phenotyping in Myopia I: Implications of Anterior Scleral Canal Opening versus Bruch's Membrane Opening Offset. AJO. 2019:43.
59. Chauhan BC, Danthurebandara VM, Sharpe GP, et al. Bruch's Membrane Opening Minimum Rim Width and Retinal Nerve Fiber Layer Thickness in a Normal White Population: A Multicenter Study. Ophthalmology. Sep 2015;122(9):1786–94. doi:10.1016/j.ophtha.2015.06.001 [PubMed: 26198806]
60. Chauhan BC, Burgoyne CF. From clinical examination of the optic disc to clinical assessment of the optic nerve head: a paradigm change. AJO. Aug 2013;156(2):218–227 e2. doi:10.1016/j.ajo.2013.04.016
61. He L, Ren R, Yang H, et al. Anatomic vs. acquired image frame discordance in spectral domain optical coherence tomography minimum rim measurements. PLoS One. March 18 2014;9(3):e92225. doi:10.1371/journal.pone.0092225 [PubMed: 24643069]
62. Spaide RF. Enhanced depth imaging optical coherence tomography of retinal pigment epithelial detachment in age-related macular degeneration. AJO. Apr 2009;147(4):644–52. doi:10.1016/j.ajo.2008.10.005
63. Luo H, Yang H, Gardiner SK, et al. Factors Influencing Central Lamina Cribrosa Depth: A Multicenter Study. IOVS. May 1 2018;59(6):2357–2370. doi:10.1167/iovs.17-23456
64. Yang H, Luo H, Gardiner SK, et al. Factors Influencing Optical Coherence Tomography Peripapillary Choroidal Thickness: A Multicenter Study. IOVS. Feb 1 2019;60(2):795–806. doi:10.1167/iovs.18-25407
65. Strouthidis NG, Yang H, Fortune B, Downs JC, Burgoyne CF. Detection of optic nerve head neural canal opening within histomorphometric and spectral domain optical coherence tomography data sets. IOVS. Jan 2009;50(1):214–23. doi:10.1167/iovs.08-2302
66. Holm S A Simple Sequentially Rejective Multiple Test Procedure. Scandinavian Journal of Statistics. 1979;6(2):65–70.
67. Helmholtz HV. Description of an ophthalmoscope for examining the retina in the living eye. AMA Arch Ophthalmol. Nov 1951;46(5):565–83. doi:10.1001/archopht.1951.01700020578016 [PubMed: 14868087]
68. Huang D, Swanson EA, Lin CP, et al. Optical coherence tomography. Science. Nov 22 1991;254(5035):1178–81. [PubMed: 1957169]
69. Gmeiner JM, Schrems WA, Mardin CY, Laemmer R, Kruse FE, Schrems-Hoesl LM. Comparison of Bruch's Membrane Opening Minimum Rim Width and Peripapillary Retinal Nerve Fiber Layer Thickness in Early Glaucoma Assessment. IOVS. Jul 1 2016;57(9):OCT575–84. doi:10.1167/iovs.15-18906
70. See JL, Nicolela MT, Chauhan BC. Rates of neuroretinal rim and peripapillary atrophy area change: a comparative study of glaucoma patients and normal controls. Ophthalmology. May 2009;116(5):840–7. doi:10.1016/j.ophtha.2008.12.005 [PubMed: 19410941]
71. Jonas JB, Fernandez MC, Sturmer J. Pattern of glaucomatous neuroretinal rim loss. Ophthalmology. Jan 1993;100(1):63–8. [PubMed: 8433829]

72. Quigley HA, Green WR. The histology of human glaucoma cupping and optic nerve damage: clinicopathologic correlation in 21 eyes. Ophthalmology. Oct 1979;86(10):1803–30. [PubMed: 553256]

73. Quigley HA, Addicks EM, Green WR. Optic nerve damage in human glaucoma. III. Quantitative correlation of nerve fiber loss and visual field defect in glaucoma, ischemic neuropathy, papilledema, and toxic neuropathy. Arch Ophthalmol. Jan 1982;100(1):135–46. [PubMed: 7055464]

74. Yang H, Luo H, Hardin C, et al. Optical Coherence Tomography Structural Abnormality Detection in Glaucoma Using Topographically Correspondent Rim and Retinal Nerve Fiber Layer Criteria. AJO. 2019;213:203–216.

75. Hayreh SS. Blood supply of the optic nerve head and its role in optic atrophy, glaucoma, and oedema of the optic disc. BJO. Nov 1969;53(11):721–48.

76. Kim TW, Kim M, Weinreb RN, Woo SJ, Park KH, Hwang JM. Optic disc change with incipient myopia of childhood. Ophthalmology. Jan 2012;119(1):21–6 e1–3. doi:10.1016/j.ophtha.2011.07.051 [PubMed: 21978594]

77. Kim M, Choung HK, Lee KM, Oh S, Kim SH. Longitudinal Changes of Optic Nerve Head and Peripapillary Structure during Childhood Myopia Progression on OCT: Boramae Myopia Cohort Study Report 1. Ophthalmology. Aug 2018;125(8):1215–1223. doi:10.1016/j.ophtha.2018.01.026 [PubMed: 29550000]

78. Lee KM, Choung H-K, Kim M, Oh S, Kim SH. Positional Change of Optic Nerve Head Vasculature during Axial Elongation as Evidence of Lamina Cribrosa Shifting: Boramae Myopia Cohort Study Report 2. Ophthalmology. 2018;125(8):1224–1233. doi:10.1016/j.ophtha.2018.02.002 [PubMed: 29544962]

79. Kim YW, Choi JJ, Girard MJA, Mari JM, Choi DG, Park KH. Longitudinal Observation of Border Tissue Configuration During Axial Elongation in Childhood. IOVS. Apr 1 2021;62(4):10. doi:10.1167/iovs.62.4.10

80. Zangalli C, Costa VP. OCT detected optic nerve head remodeling in a young adult with early progressive myopia. Am J Ophthalmol Case Rep. Jun 2022;26:101535. doi:10.1016/j.ajoc.2022.101535 [PubMed: 35509283]

81. Helb HM, Charbel Issa P, Fleckenstein M, et al. Clinical evaluation of simultaneous confocal scanning laser ophthalmoscopy imaging combined with high-resolution, spectral-domain optical coherence tomography. Acta Ophthalmol. Dec 2010;88(8):842–9. doi:10.1111/j.1755-3768.2009.01602.x [PubMed: 19706019]

82. Strouthidis NG, Yang H, Reynaud JF, et al. Comparison of clinical and spectral domain optical coherence tomography optic disc margin anatomy. IOVS. Oct 2009;50(10):4709–18. doi:10.1167/iovs.09-3586

83. Zheng F, Wu Z, Leung CKS. Detection of Bruch's Membrane Opening in Healthy Individuals and Glaucoma Patients with and without High Myopia. Ophthalmology. Oct 2018;125(10):1537–1546. doi:10.1016/j.ophtha.2018.04.031 [PubMed: 29934269]

84. Strouthidis NG, Yang H, Downs JC, Burgoyne CF. Comparison of clinical and three-dimensional histomorphometric optic disc margin anatomy. IOVS. May 2009;50(5):2165–74. doi:10.1167/iovs.08-2786

85. Rezapour J, Proudfoot JA, Bowd C, et al. Bruch Membrane Opening Detection Accuracy in Healthy Eyes and Eyes With Glaucoma With and Without Axial High Myopia in an American and Korean Cohort. AJO. May 2022;237:221–234. doi:10.1016/j.ajo.2021.11.030

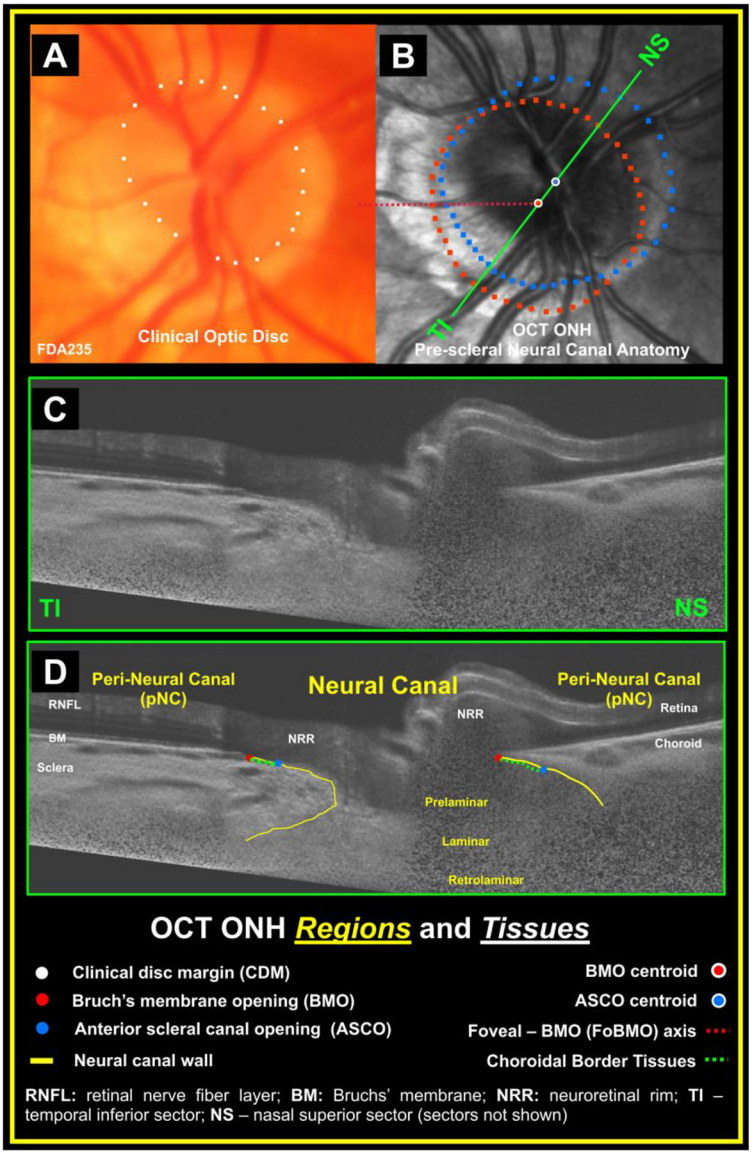

Figure 1. OCT-detected anatomy defines the ONH neural canal and peri-neural canal (pNC) regions and tissues.

(A) The clinical "optic disc" (or "papilla") and "peripapillary" regions are defined relative to the clinical disc margin (see Supplemental Figure 1). (B) We propose that OCT examination of the ONH tissues should be organized relative to the OCT-detected Bruch's Membrane Opening (BMO) and neural canal. We define the neural canal to be the connective tissue pathway through the choroid and sclera through which the RGC axon bundles achieve the retrolaminar orbital optic nerve. The pre-scleral neural canal extends from BMO to the anterior scleral canal opening, (ASCO) and is lined by the choroidal border tissues of Elschnig (henceforth the CBT).(refs) The scleral portion of the neural canal extends from the ASCO through the scleral flange opening (SFO) (when present - see Figures 2–6) and ends at the posterior scleral canal opening which is, at present, inconsistently visualized by OCT and is not segmented here see (Figures 5 and 6). (C) OCT-radial B-scan from the location depicted by the green line in Panel B. (D) ONH neural canal tissues are contained within

the neural canal and ONH pNC tissues are peripheral, (but immediately adjacent to), BMO and the neural canal wall. We propose these terms so as to distinguish OCT ONH anatomic terminology from the clinical terms optic disc, papilla, and peri-papillary which have no consistent anatomic foundation (see Supplemental Figure 1). (Reprinted with minor edits from Burgoyne et al, AJO, 2023).[13]

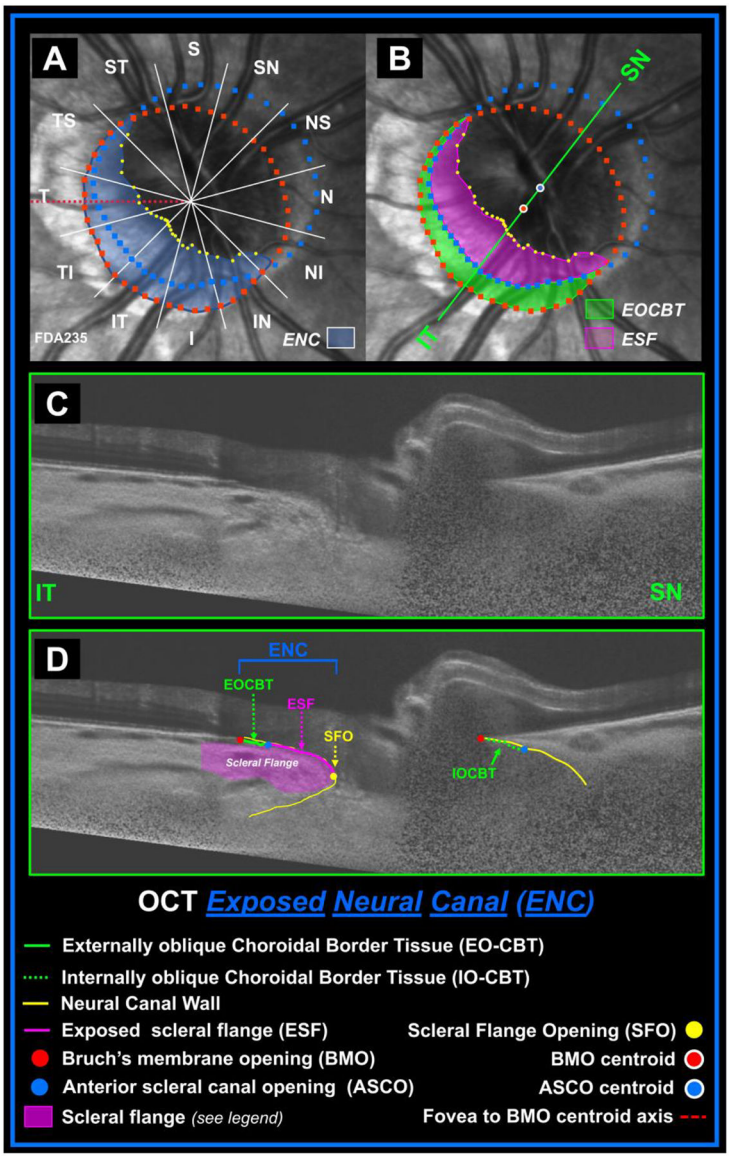

Figure 2. OCT exposed neural canal (ENC) region morphology (A) includes externally oblique choroidal border tissue (EOCBT) and/or exposed scleral flange (ESF) (B, C and D) sub-regions.

(A) Pre-scleral and scleral flange neural canal anatomy projected onto the fundus photo of study eye FDA235, (also shown in Figure 1). In this eye the ENC region is longest inferior temporally and extends from Bruch's membrane opening (BMO–red dots) to the scleral flange opening (SFO-yellow dots). OCT anatomic landmarks are shown relative to the Foveal-to-BMO centroid (FoBMO) axis and 12 FoBMO 30° sectors (sectoral acronyms defined below). (B) The EOCBT sub-region is shown in translucent green and the adjacent ESF sub-region is shown in translucent magenta (also seen on the left of Panels C and D). (C) OCT-radial B scan from the location depicted by the green line in Panel B. (D) The scleral flange histologically refers to the region of the pNC-sclera that is internal to the insertion of the dural sheath.[14,16,29,30] Because, the dural sheath is not consistently visualized in OCT B-scans, the outer boundary of the scleral flange cannot (yet) be consistently determined by OCT. We hypothesize that EOCBT and ESF regions are a

manifestation of neural canal remodeling that is required when BMO enlarges and/or shifts temporally relative to the ASCO and SFO (when present) (Figures 2, 4, 12 and 13). IOCBT - internally oblique choroidal border tissues (BMO central to the ASCO) (right side of Panels C and D); FoBMO 30° sectoral acronyms (Panel A): S-superior; SN-superior-nasal; NS-nasal-superior; N-nasal; NI-nasal-inferior; IN-inferior-nasal; I-Inferior; IT-Inferior-temporal; TI-temporal-inferior; T-temporal; TS-temporal-superior; ST-superior-temporal.

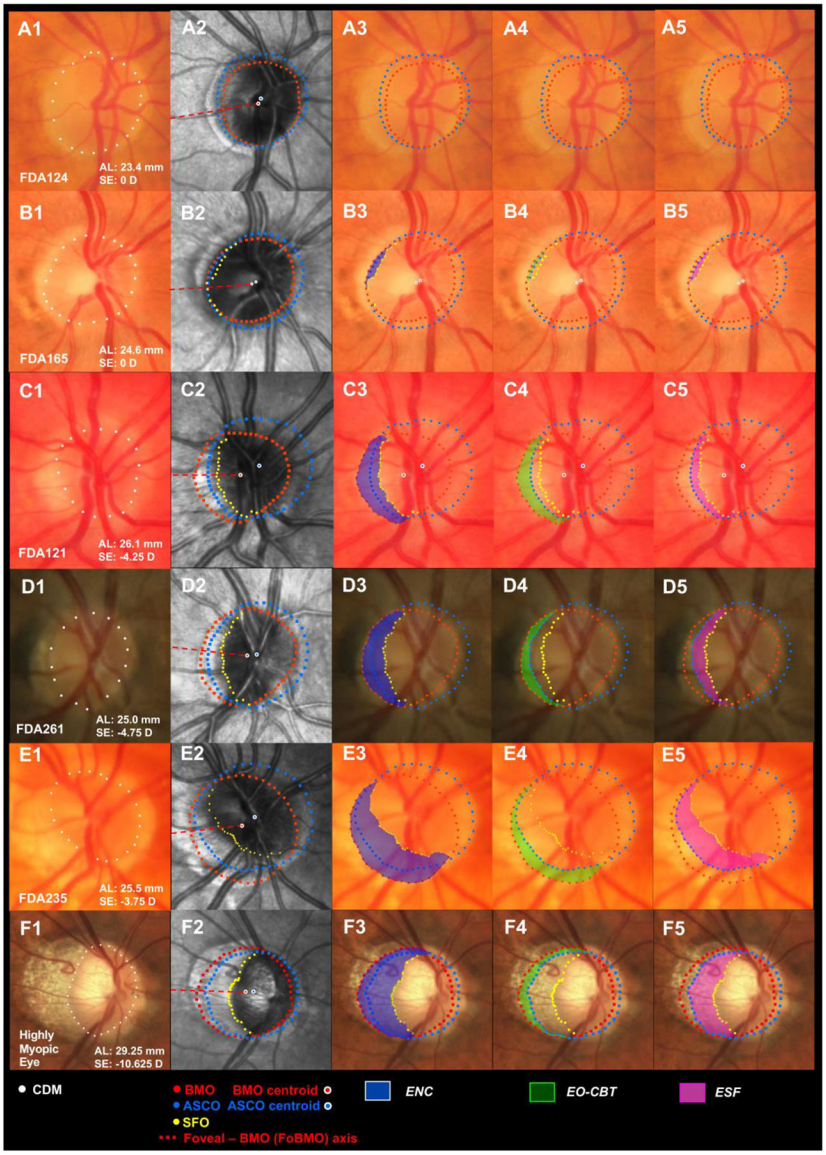

Figure 3. Exposed neural canal (ENC) regions occur through the full spectrum of non-highly myopic, myopia.

Five non-highly myopic study eyes (Panels A2–E5) demonstrate the range of ENC region size found in this study (non-existent in (A) and close to the largest in (E)). Panels F1–F5 demonstrate a representative highly myopic eye that is shown for context but was not included in this study. The eyes demonstrate a range of spherical equivalent (SE) refractive error and axial length (AL) that only loosely correlate with ENC region size. (A1–F1) Clinical optic nerve head (ONH) photograph of each eye with an estimate of the clinical disc margin (CDM) outlined by white points. (A2–F2) OCT prelaminar neural canal anatomy (Bruch's membrane opening (BMO), anterior scleral canal opening (ASCO) and the scleral flange opening (SFO), (where applicable), projected onto the scanning laser ophthalmoscopic (SLO) infrared (IR) image associated with each OCT data set. (A3–F3) Prelaminar neural canal landmarks projected onto an ONH photograph of each eye after it has been colocalized to the SLO IR image using the retinal vasculature. The ENC region

in each eye (absent in (A3)) is identified by a translucent blue crescent. (A4–F4) The ENC region may include both an Externally Oblique Choroidal Border Tissue (EOCBT) sub-region (absent in A4) which in some eyes is accompanied by an adjacent Exposed Scleral Flange (ESF) sub-region (translucent magenta) (panels B5–F5). Figure 4 shows representative OCT anatomy for each eye of this figure.

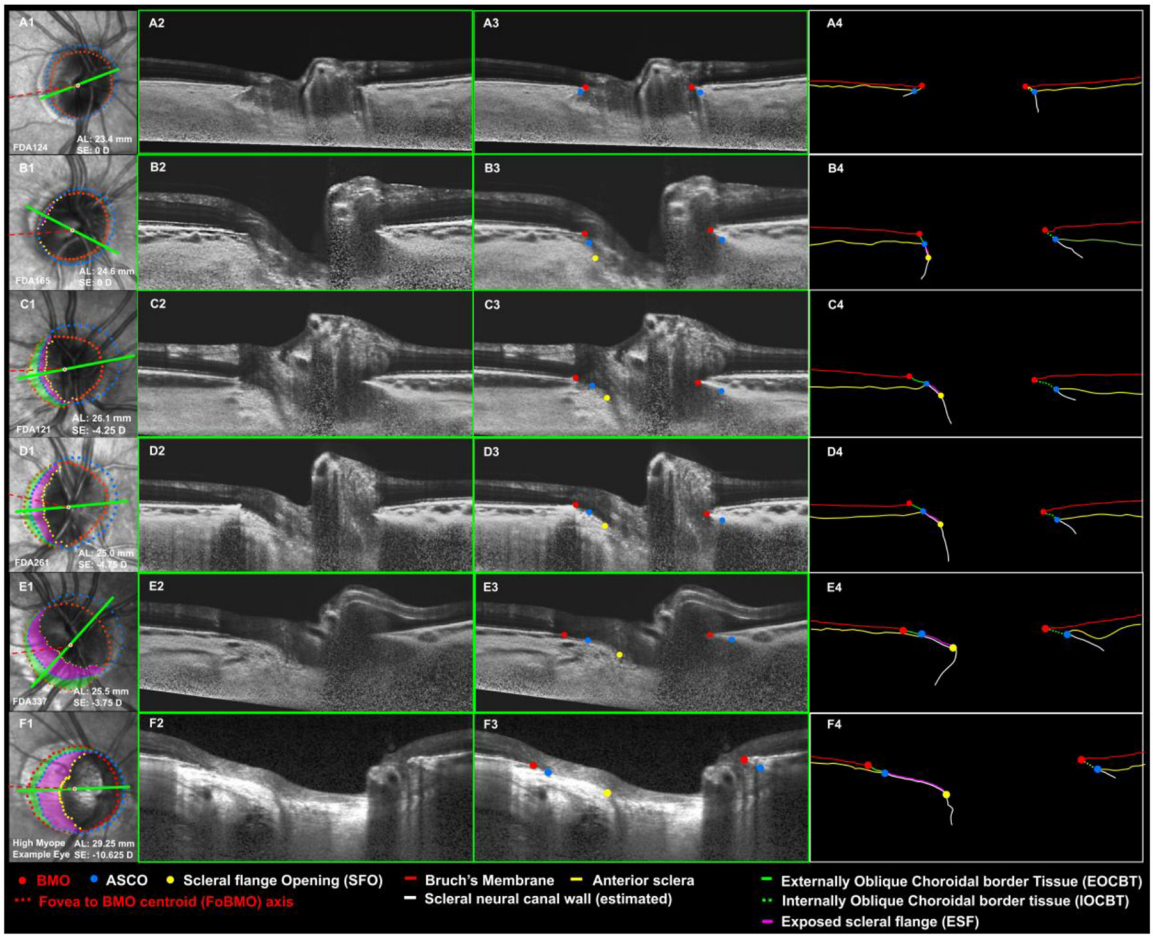

Figure 4. OCT exposed neural canal (ENC) region anatomy and segmentation.

(A1–F1) radial location of the OCT B-scan shown in Panels A2–F2 and A3–F3. (A2–F2) OCT B-scans from the locations denoted by a green line in panels A1–F1. (A3–F3) OCT ENC region anatomic landmarks. (A4–F4) Pertinent ENC region and EOCBT and ESF sub-region segmentations. We define an EOCBT region to be internal to BMO extending to the ASCO which defines the CBT insertion into the scleral flange. We define an ESF region to extend from the ASCO to the SFO and to be devoid of overlying choroid and/or Bruch's membrane. (A1–A4) Study eye FDA124 does not demonstrate an ENC region because the CBTs are internally oblique in all ONH segments (Figure 2, panel D). (B1–B4) FDA165 demonstrates very thin EOCBT and ESF regions. ((C1)–(E4)) Panels C – E show three non-highly myopic eyes with the largest ENC regions by radial and sectoral extent. The ENC region of each eye contains both EOCBT and ESF sub-regions. (F1–F4) Panel F contains an example highly myopic eye (not included in this study), in which the ESF region is even further elongated.

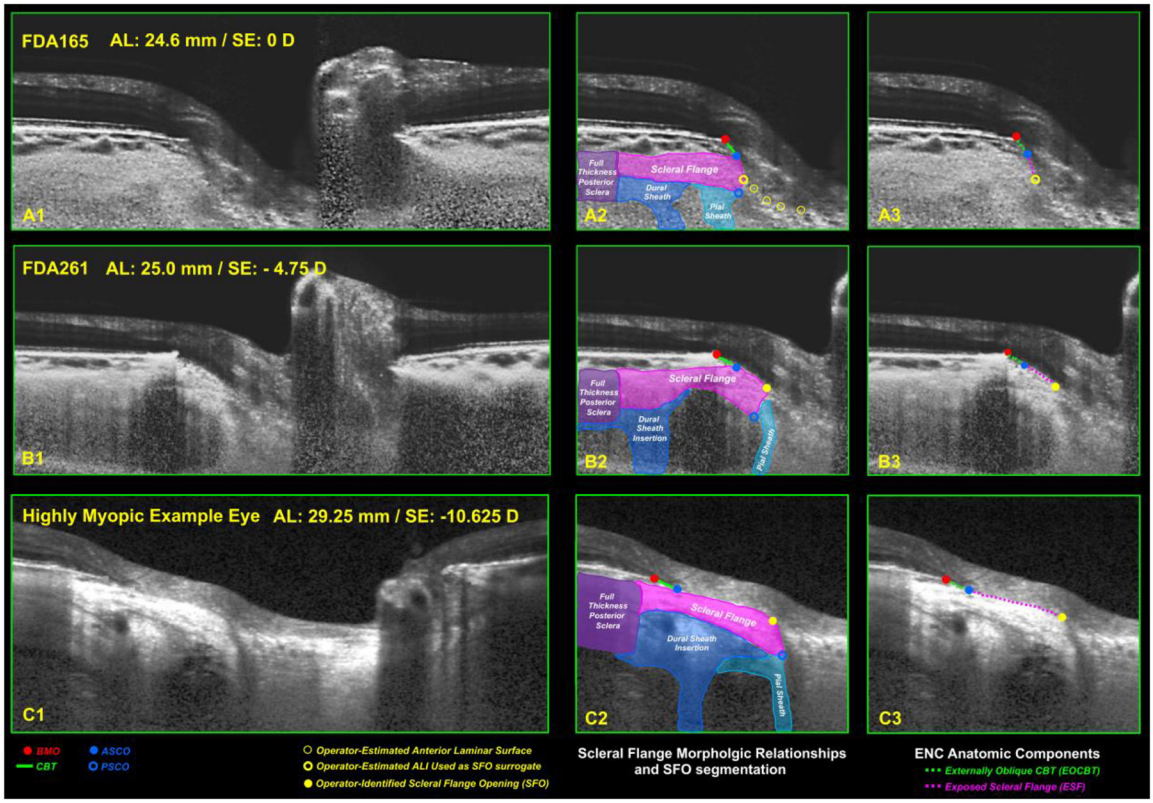

Figure 5. OCT scleral flange anatomy, morphologic relationships, scleral flange opening (SFO) segmentation and parameterization.

(A1 – C1) See Figures 3 and 4 for the clinical location of the three B-scans in these panels (FDA165 (A1) top, FDA261 (B1) middle, and Highly Myopic Example eye, (C1) bottom). (A2 – C2) The scleral flange histologically refers to the peri-neural canal (pNC) sclera that is “central “or “internal” to the dural sheath insertion. The dural sheath adds substantial thickness to the outer layers of the posterior sclera. The potential thinness of the scleral flange relative to the adjacent posterior sclera may have important biomechanical implications on the flow of blood within the posterior ciliary arteries which pass through the scleral flange to achieve the juxta canalicular choroid as well as the lamina cribrosa. The anterior scleral canal opening (ASCO) is histologically defined to be the projection of the anterior scleral flange surface through the choroidal border tissues (CBT). The posterior scleral canal opening has been described histologically and using 3D histomorphometry (see Introduction) but is not consistently visualized in OCT imaging and is shown here for representation purposes only. For this study the scleral flange opening (SFO) was manually segmented by a single operator (SWH) either “geometrically” when identifiable (Panels B2 and C2, see Methods) or, when not geometrically identifiable, estimated visually by projecting the anterior laminar surface through the neural canal wall (Panel A2, see methods). (A3 – C3) Existing BMO and ASCO segmentations in combination with the newly segmented SFO points were used to define the externally oblique CBT (EOCBT) and Exposed Scleral Flange (ESF) sub-regions of the ENC region which were parameterized within BMO reference plane as shown in Figures 6 and 7.

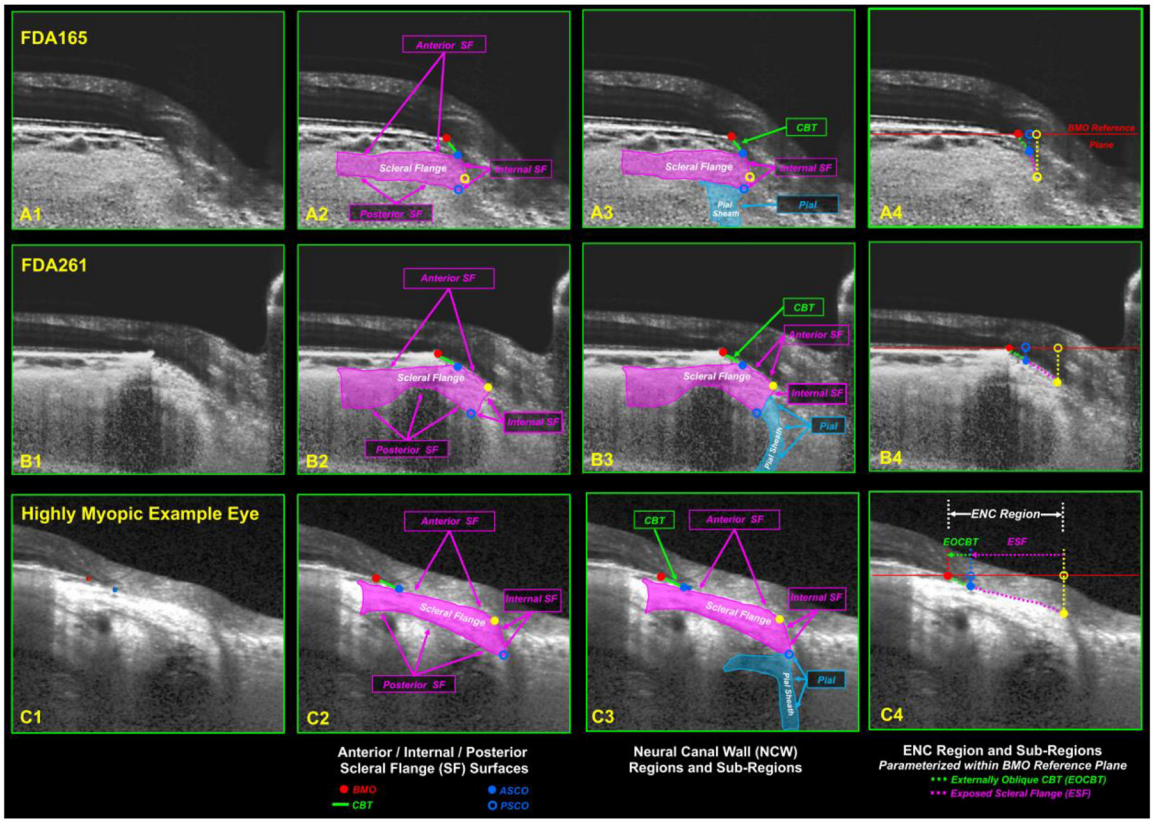

Figure 6. OCT Scleral Flange Surfaces, Neural Canal Wall Regions and Exposed Neural Canal Region parameterization within Bruch's Membrane Opening (BMO) reference plane.

(A1 – C1, left) See Figure 5 for additional context. See Figures 3 and 4 for the clinical photos and ONH location of the B-scans for each eye: FDA165 (A1) top, FDA261 (B1) middle, and a Highly Myopic Example eye, (C1) bottom). (A2 – C2) Morphologic variation in the anterior, internal and posterior scleral flange surfaces are illustrated (see Supplemental Table 1). Unlike the anterior and internal surfaces which can be histologically defined, the posterior scleral flange "surface" and "peripheral" extent of the scleral flange cannot be histologically determined and should be considered a biological continuum. (A3 – C3) We define the neural canal to extend from BMO through the posterior scleral canal opening (PSCO) with a variable transition into the orbital pial sheath. Morphologic variation in the CBT, anterior scleral flange, internal scleral flange and pial portions of the neural canal are demonstrated. (A4 – C4) In this study, measurement of the exposed neural canal (ENC), externally oblique choroidal border tissue (EO-CBT), and the exposed scleral flange (ESF) regions was performed after projection of all segmented BMO, ASCO and SFO points to the BMO reference plane (A4 – C4) (see Methods).

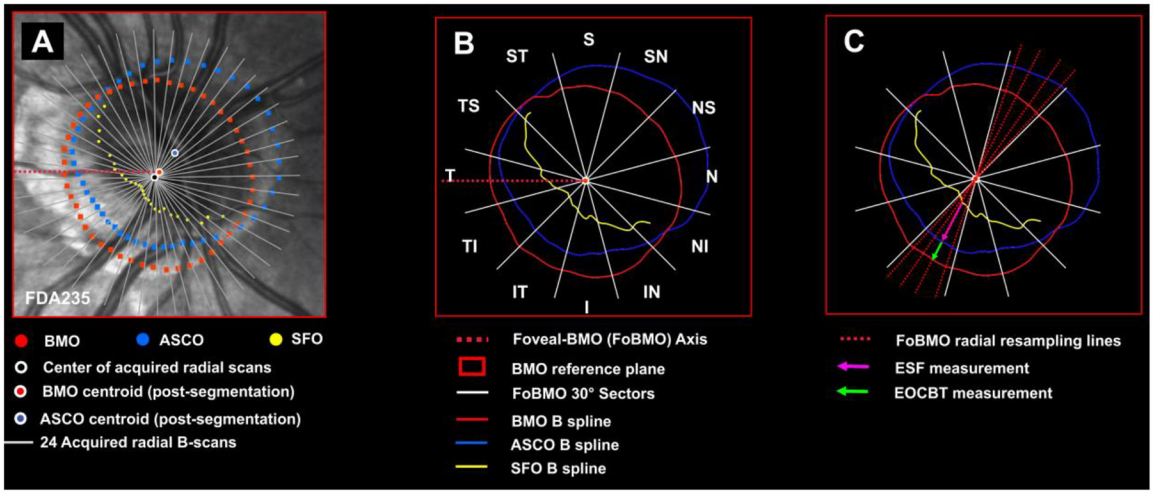

Figure 7. Projecting Bruch's membrane opening (BMO), anterior scleral canal opening (ASCO) and scleral flange opening (SFO) points to the BMO reference plane allows externally oblique choroidal border tissue (EOCBT) and exposed scleral flange (ESF) sub-region measurements to be made relative to the Foveal to BMO centroid (FoBMO) axis and within FoBMO 30° sectors.

(A) The center of the acquired radial B-scan scans (white circle with black center does not always coincide with the post-BMO segmentation, anatomic BMO centroid (red circle with white outline–see Methods). By projecting the BMO, ASCO and SFO points to the BMO reference plane for measurement, the centroid of the segmented BMO points can be used to establish anatomically consistent FoBMO 30° sectors as shown in (B). (B) BMO, ASCO and SFO B splines plotted within the BMO reference plane relative to the FoBMO axis and 30° sectors (white lines). (C) ESF, EOCBT and ENC region (ENC = ESF + EOCBT) measurements can then be made within four equidistance re-sampling lines within each 30° sector and averaged. Data from sectors with < 2 measurements were not included. See Figure 2 for the 30° sectoral acronym names shown in Panel B.

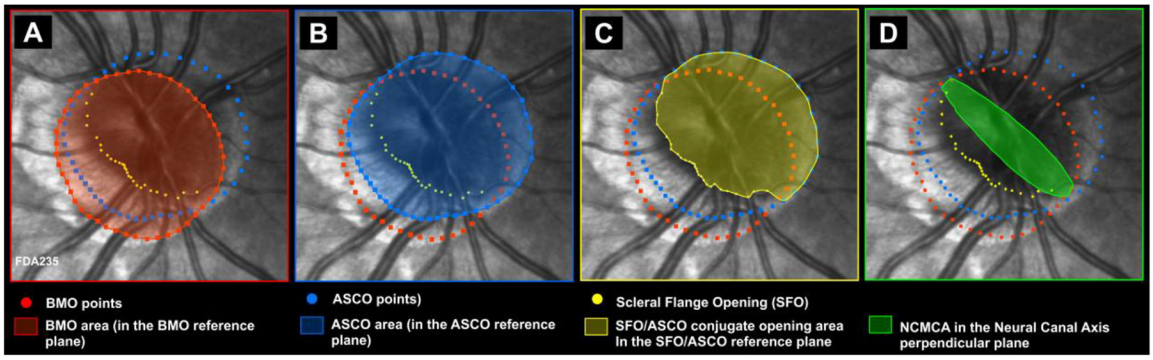

Figure 8. The size and shape of three neural canal openings as well as the estimated Neural Canal Minimum Cross-Sectional Area in a representative study eye (FDA235).

(A) Bruch's membrane opening (BMO), (B) the anterior scleral canal opening (ASCO), (C) the scleral flange opening/anterior scleral canal opening (SFO/ASCO) conjugate opening and (D) Neural Canal Minimum Cross-Sectional area (NCMCA) which is an estimate of the smallest dimension of the pre-scleral neural canal through which the retinal ganglion cell axons pass (see Methods and Supplemental Figure 4). For the three openings shown, their size and shape (ovality index) were assessed using a best-fit ellipse within their respective best fit reference plane. (ref) The 48 ASCO/SFO conjugate opening points (24 radials, 2 points per radial) consist of the SFO points where present, and the ASCO points at the radial locations where an SFO point is not present. The NCMCA is calculated within the pre-scleral neural canal axis perpendicular plane (see Supplemental Figure 2). The sizes and shapes of each opening cannot be accurately compared in this Figure. They must be seen within a common viewing plane and positioned relative to a common centroid and common long axis to be directly comparable (see Supplemental Figure 8).

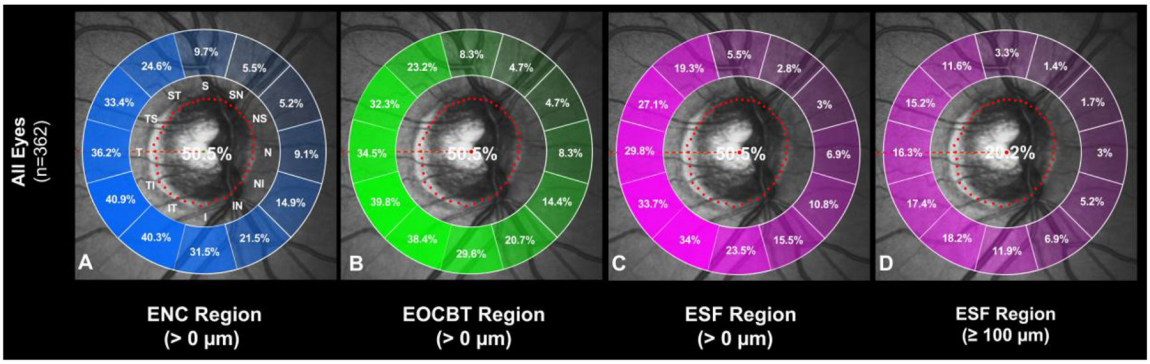

Figure 9. The sectoral prevalence of the ENC (A), EOCBT (B), and ESF regions (C) in eyes in which they are > 0 µms as well as the sectoral prevalence of an ESF region that is ≥ 100 µms (D) among all study eyes are shown.

For (A, B and C) sectoral data are the percent of 362 eyes in which an ENC, EOCBT or ESF > 0 µm is present in a given sector. Panel (D) reports the sectoral prevalence of an ESF region ≥100 µm among all study eyes. All data are in right eye orientation as shown in Panel A. See Figure 2 legend for the definition of the Panel A 30° sectoral acronyms.

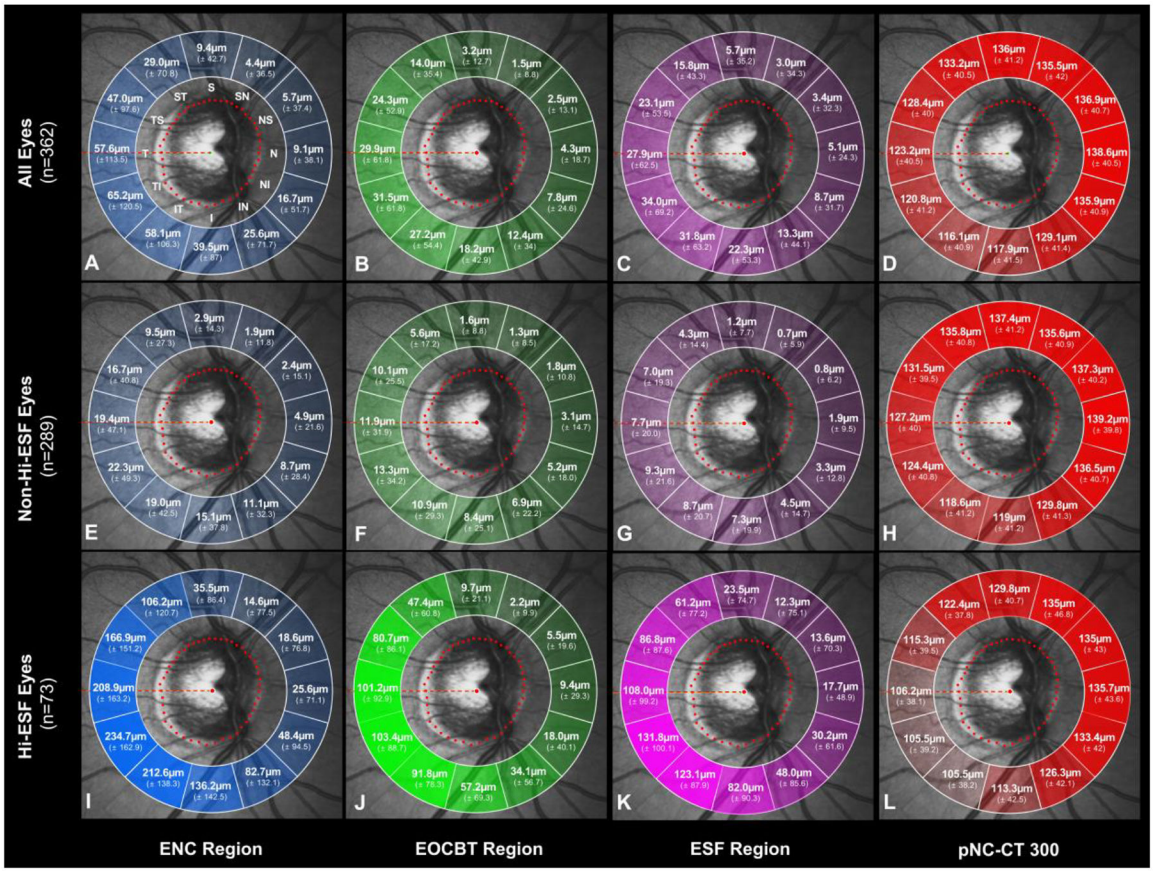

Figure 10. FoBMO 30° sectoral mean (± standard deviation) length of the exposed neural canal (ENC) (left), externally oblique choroidal border tissue (EOCBT) (mid-left), and exposed scleral flange (ESF) (mid-right) regions as well as peri-neural canal choroidal thickness (pNC-CT) at the 300 μm measurement point (right) within: all Study Eyes (upper row); Non-Hi-ESF eyes (0 ≤ ESF < 100 μms) (middle row); and Hi-ESF eyes (ESF ≥ 100 μms) (bottom row).

Within this analysis, data for each eye and each ENC region includes the average sectoral values for that region in each sector (with sectoral values in which there is no ENC, no EOCBT or no ESF, (respectively) being treated as zero (0)). All data are in right eye orientation (upper left panel (see Figure 2 legend for the sectoral acronym definitions). See Supplemental Figure 6 for pNC-CT measurement data at the 100, 700 and 1100 um measurement points which confirm that the inferior temporal thinning shown in the pNC-CT 300 data extends to all pNC-CT measurement points.

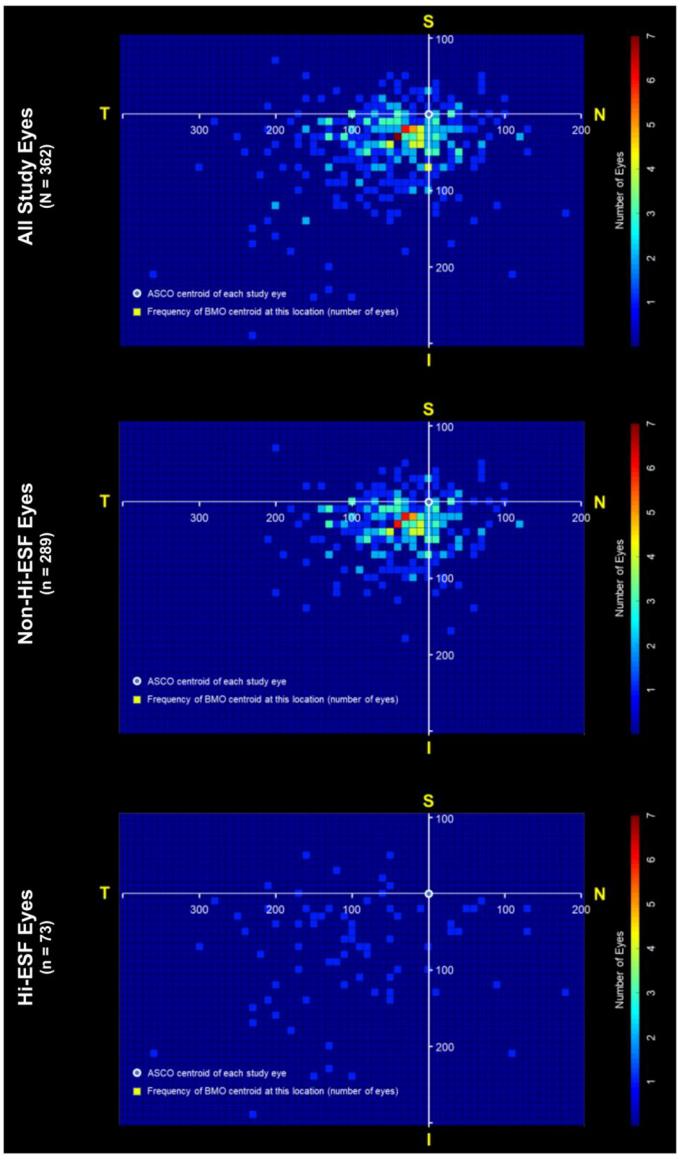

Figure 11. The frequency and location of BMO centroid offset relative to the ASCO centroid (BMO/ASCO offset) within: all 362 study eyes (A); all Non-Hi-ESF (n=289) eyes (B); and all Hi-ESF (n=73) eyes (C).

For each group of eyes, data are a 2D plot of the frequency and location of the BMO centroid relative to the ASCO centroid, (after projection to the BMO reference plane). The number of eyes at a given location is depicted by the color scale to the right. The ASCO centroid of each eye (blue circle with white outline) is located at the origin (0, 0) of the data plot. All data are in right eye, FoBMO orientation. (temporal - T; superior - S; nasal - N; inferior - I). These data suggest that the greatest frequency and magnitude of BMO/ASCO offset occurs within the inferior-temporal quadrant and that the largest BMO/ASCO offset occurs almost exclusively in the Hi-ESF eyes.

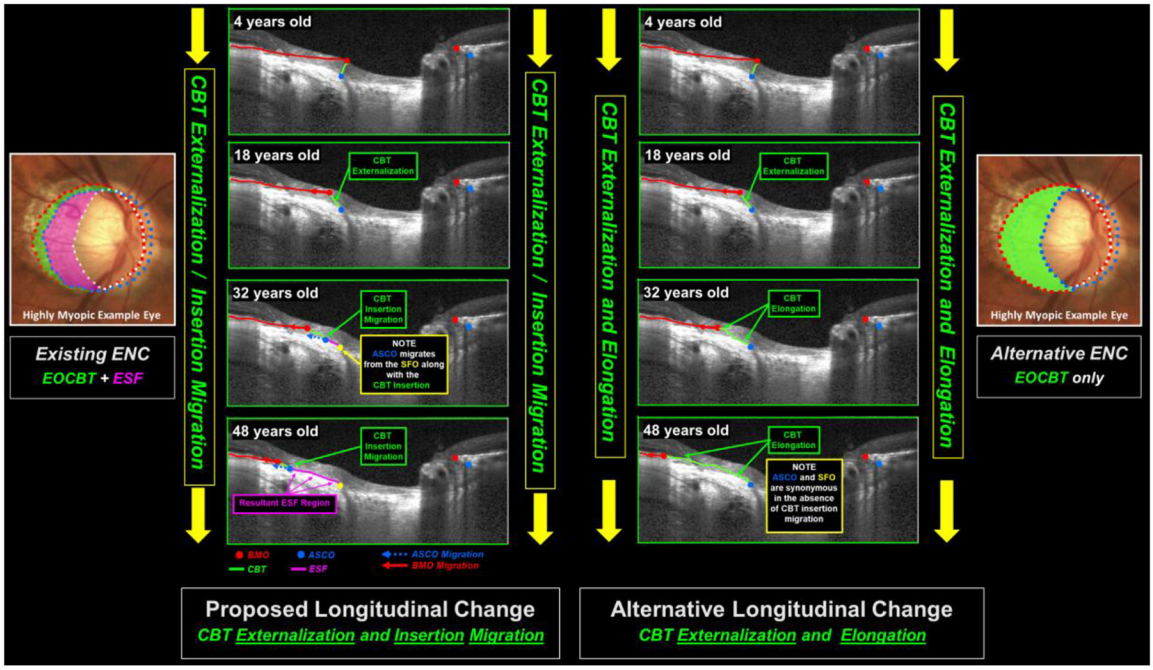

Figure 12. We propose that the primary posterior scleral, scleral flange, choroidal and retinal remodeling of axial myopia cause or are accompanied by primary and secondary optic nerve head (ONH) neural canal remodeling that can be highly variable among eyes at all axial lengths.

Here the existing exposed neural canal (ENC) region from the 48-year-old Highly Myopic Example Eye from Figures 3 – 6 (Left Panel) is used to create a "Proposed Longitudinal Change" scenario (Left Middle Panels) in which choroidal border tissue (CBT) "externalization" and "insertion migration" away from the original anterior scleral canal opening (ASCO) leaves a region of exposed scleral flange (ESF) and a geometrically identifiable scleral flange opening (SFO). This suggests that in the setting of CBT migration away from the SFO, the SFO is synonymous with the ASCO prior to the onset of neural canal remodeling. However, an "Alternative Longitudinal Change" scenario (Right Middle Panels) can be imagined, (based on the appearance of other highly myopic eyes (not shown)), in which the CBT is externalized and elongates progressively without losing its insertion into the original ASCO. (Right Panel) Had CBT elongation alone occurred, the expected composition of the ENC region would consist entirely of an EOCBT region only – without creating an ESF region.

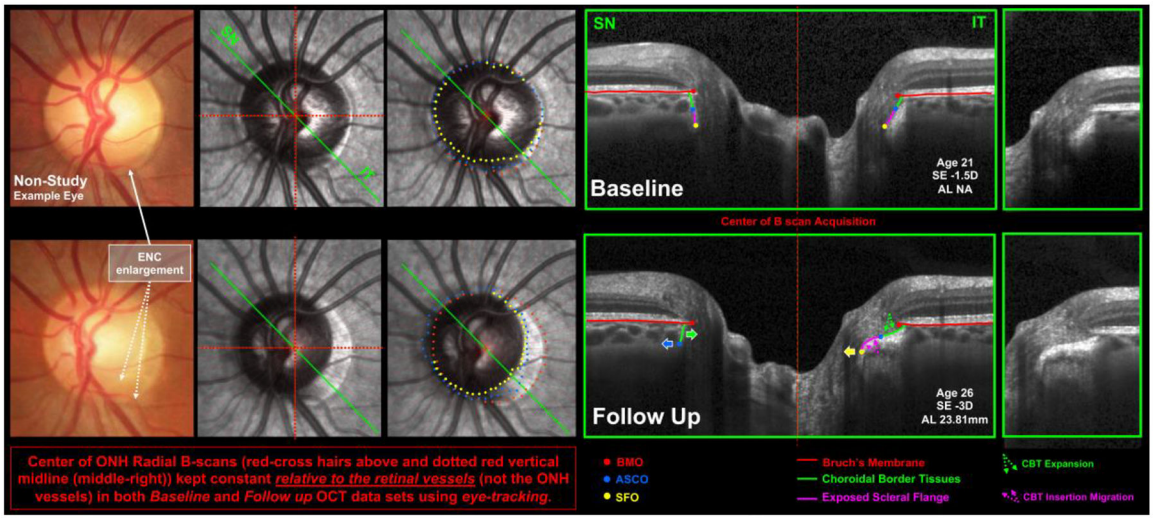

Figure 13. Longitudinal OCT imaging in a previously reported[80] mildly myopic eye undergoing early optic nerve head (ONH) neural canal remodeling demonstrates inferior-temporal (IT) expansion of an exposed neural canal (ENC) region that includes choroidal border tissue (CBT) insertion migration, CBT extension and the suggestion of neural canal contraction and shape change.

(Far-Left) Color ONH photos of a non-study left eye (Baseline (above) and Follow Up (below)) presented in native left eye orientation, demonstrate inferior-temporal expansion of the clinically visible exposed neural canal (ENC) region (dotted white arrows, below). (Middle-Left) Infrared (IR) image acquired at the time of OCT radial B-scan acquisition. Because Heidelberg Engineering Spectralis Baseline and Follow Up images are acquired using eye-tracking software that uses the retinal (rather than the ONH) vasculature to keep the center of radial B-scan acquisition constant, the position of the center of radial B-scan acquisition (red-dotted cross-hairs) is stable relative to the retina, isolating the movement of the deep ONH tissues relative to it (and thus relative to BMO). Note that the clinical "shadow" of the neural canal appears smaller, more oval in shape and is superior-nasally displaced in the Follow Up image. The green line identifies the position of the B-scan to the right (SN – superior-nasal; IT- inferior-temporal). (Middle) Same IR images as to the left, with Bruch's Membrane Opening (BMO – Red dots), Anterior Scleral Canal Opening (ASCO – Blue dots) and Scleral Flange Opening (SFO – Yellow dots) segmentations projected onto the BMO reference plane. Note that the ASCO and SFO openings are shifted superior nasally, contracted and ovalized in the Follow Up compared to the Baseline images. (Middle-Right), Representative Baseline and Follow Up B-scans acquired at the same location relative to the retinal vessels (Center of B Scan Acquisition - red dotted vertical line) showing BMO, ASCO, and SFO points as well as Bruch's Membrane, (red line), CBT (green line) and Exposed Scleral Flange (magenta line) on both the SN (left) and IT (right) sides of the canal. Note that while BMO does not appear to be altered in size or position within the Follow Up image, the ASCO and SFO points are shifted nasally relative to BMO. On the SN side of the canal, (left) the nasal displacement of the ASCO (blue arrow) relative to BMO has resulted in "internalization" of the CBT (i.e., changing from "externally" to "internally" oblique – (green arrow)) (refs) and the loss of an identifiable SFO and ESF region (because BM now overlies this portion of the scleral flange). On the IT side of the canal, (right), the SFO is profoundly nasally displaced relative to BMO

(yellow arrow), CBT morphology alterations including modest CBT insertion migration (dotted magenta arrows) and substantial CBT extension (dotted green arrows) have occurred. (Far-Right) Enlarged and unsegmented IT scleral flange anatomy for reference.

Table 1.

Acronyms and Definitions.

Acronyms and Definitions	
ASCO	Anterior Scleral Canal Opening
BM	Bruch's Membrane
BMO	Bruch's Membrane Opening
CBT	Choroidal Border Tissues
CCT	Central Corneal Thickness
CDM	Clinical Disc Margin
ENC	Exposed Neural Canal (ONH region)
EOCBT	Externally Oblique Choroidal Border Tissues (ONH region)
ESF	Exposed Scleral Flange (ONH region)
FDA	Food and Drug Administration – 1st 3 letters of study subject ID number
FoBMO	Foveal–BMO Centroid
Hi-ESF	Study Eyes in which the ESF region is ≥ 100 μms in at least one sector
ICC	Intraclass Correlation Coefficient
ID	Identification - as in study subject "ID" number
IOCBT	Internally Oblique Choroidal Border Tissues
NC	Neural Canal
NCMCA	Neural Canal Minimum Cross-Sectional Area (Supplemental Figure 2)
Non-Hi-ESF	Study eyes in which the ESF region is < 100 μms in all sectors
OCT	Optical Coherence Tomography
ONH	Optic Nerve Head
pNC	Perineural Canal
pNC-CT	Perineural Canal Choroidal Thickness
PSCO	Posterior Scleral Canal Opening (Not segmented in this study)
RNFL	Retinal Nerve Fiber Layer
RNFLT	Retinal Nerve Fiber Layer Thickness
RPE	Retinal Pigment Epithelium
Sector	ONH FoBMO 30° (clock-hour) sectors (see Figure 2, Panel (A))
SFO	Scleral Flange Opening
SD	Standard Deviation
SE	Spherical Equivalent

Table 2.

Demographic, ocular, neural canal and pNC-CT characteristics of the study participants shown for three groups: All Study Eyes (left), Non-Hi-ESF eyes (0 ≤ ESF < 100 μm) (middle) and Hi-ESF eyes (ESF ≥ 100 μm) eyes (right).

	All Study Eyes ***(n=362)***	**Non-Hi-ESF Eyes** ***(n=289)***	**Hi-ESF Eyes** ***(n=73)***	***p value*** [a]
Female Gender (n (%))	**202** (55.8)	**165** (57.09)	**37** (50.69)	.394
Left Eye (n (%))	**181** (50)	**147** (50.87)	**34** (46.58)	.600
Age (year ± SD, (range))	**50.62 ± 17.53** (19 to 90)	**50.28 ± 16.97** (19 to 90)	**51.96 ± 16.92** (20 to 84)	.453
Axial Length (mm ± SD, (range))	**23.74 ± 0.95** (21.41 to 26.44)	**23.64 ± 0.88** (21.41 to 26.44)	**24.15 ± 1.11** (21.96 to 26.29)	**<.001** [a]
Spherical Equivalent (diopter ± SD, (range))	**−0.47 ± 1.82** (−6.00 to 5.375)	**−0.24 ± 1.53** (−5.75 to 5.375)	**−1.38 ± 2.48** (−6.00 to 4.125)	**<.001** [a]
IOP (mmHg ± SD, (range))	**14.53 ± 2.7** (7 to 21)	**14.62 ± 2.72** (9 to 21)	**14.19 ± 2.59** (7 to 21)	.218
CCT (μm ± SD, (range))	**555.31 ± 32.6** (390 to 658)	**553.58 ± 26.78** (390 to 658)	**562.14 ± 26.78** (507 to 655)	.023
BMO area (mm^2 ± SD, (range))	**1.83 ± 0.38** (1.05 to 3.46)	**1.80 ± 0.37** (1.05 to 3.46)	**1.98 ± 0.42** (1.20 to 3.15)	**.001** [a]
ASCO area (mm^2 ± SD, (range))	**2.23 ± 0.43** (1.24 to 3.97)	**2.24 ± 0.44** (1.24 to 3.97)	**2.20 ± 0.42** (1.27 to 3.43)	.477
BMO/ASCO area ratio	**0.83 ± 0.11** (0.55 to 1.21)	**0.81 ± 0.09** (0.55 to 1.12)	**0.91± 0.11** (0.66 to 1.21)	**<.001** [a]
NCMCA (mm^2 ± SD, (range))	**1.33 ± 0.42** (0.4 to 2.57)	**1.4 ± 0.38** (0.55 to 2.57)	**1.06 ± 0.44** (0.4 to 2.29)	**<.001** [a]
BMO / ASCO offset magnitude (μm ± SD, (range))	**89.76 ± 62.34** (4 to 402)	**72.6 ± 42.35** (4 to 220)	**157.71 ± 80.29** (16 to 402)	**<.001** [a]
pNC-CT 100 (μm ± SD, (range))	**108.85 ± 26.23** (45 to 194)	**109.13 ± 26.31** (45 to 194)	**106.81 ± 25.90** (65 to 175)	.612
pNC-CT 300 (μm ± SD, (range))	**129.32 ± 37.47** (37 to 244)	**131.06 ± 37.38** (37 to 244)	**121.94 ± 37.21** (62 to 220)	.074
pNC-CT 700 (μm ± SD, (range))	**156.49 ± 53.92** (36 to 296)	**160.17 ± 54.16** (36 to 296)	**141.65 ± 50.64** (57 to 273)	.008
pNC-CT 1100 (μm ± SD, (range))	**172.51 ± 62.39** (40 to 341)	**177.38 ± 62.62** (40 to 341)	**151.52 ± 57.24** (58 to 285)	**.002** [a]

[a] Statistically significant differences between the Non-Hi-ESF and Hi-ESF eyes (P < .05, t test or Chi-square test) that remain significant using a Holm-Bonferonni correction for multiple comparisons

Table 3.

Mean length (μm) of the Exposed Neural Canal (ENC), Externally Oblique Choroidal Border Tissue (EOCBT) and Exposed Scleral Flange (ESF) regions among three groups of study eyes: All Study Eyes with an ENC region (left), Non-Hi-ESF eyes (ESF < 100 μm) with an ENC region (middle) and the Hi-ESF eyes (ESF ≥ 100 μm) eyes (right).

Within each group, only eyes in which there is either an EOCBT or an ESF (the presence of either constituting an ENC) are included. Data are the mean values of the included eyes for all 12 sectors of each eye in which, for sectors in which there is no ENC, no EOCBT or no ESF, (respectively), the sectoral value is zero (0)

	All Study Eyes with an ENC *(n=183 of 362)*	Non-Hi-ESF Eyes *(n=110 of 289)*	Hi-ESF Eyes *(n=73)*	*p value* [a]
ENC *(μm ± SD, (range))*	**60.40 ± 60.11** *(1.95 to 379.36)*	**29.1 ± 20.28** *(1.95 to 133.29)*	**107.57 ± 68.98** *(28.32 to 379.36)*	**<.001**
EOCBT *(μm ± SD, (range))*	**29.08 ± 28.64** *(0.37 to 145.71)*	**17.38 ± 15.93** *(0.37 to 104.56)*	**46.71 ± 34.12** *(4.71 to 145.71)*	**<.001**
ESF *(μm ± SD, (range))*	**32 ± 37.29** *(0.31 to 236.98)*	**12.41 ± 8.38** *(0.31 to 36.94)*	**61.52 ± 44.04** *(14.56 to 236.98)*	**<.001**

[a] Statistically significant differences between the Non-Hi-ESF and Hi-ESF eyes ($p < .05$, t test)

Table 4.

Size and Shape of the BMO, ASCO, and SFO/ASCO Conjugate Openings as well as the NCMCA for All Study eyes (upper rows), Non-Hi-ESF (0 ≤ ESF < 100 μm) eyes (middle row) and Hi-ESF (ESF ≥ 100 μms) eyes (lower row).

		BMO	**ASCO**	**SFO/ASCO Conjugate Opening**	**NCMCA**
All Eyes *n=362*	Area (mm^2)	1.83 (± 0.38)	2.22 (± 0.43)	2.16 (± 0.43)	1.33 (± 0.42)
	Long axis (μm)	1609.21 (± 169.15)	1772.15 (± 176.22)	1757.96 (± 180.00)	1543.70 (± 162.88)
	Short axis (μm)	1436.64 (± 157.51)	1584.85 (± 162.46)	1557.02 (± 167.78)	1093.03 (± 290.55)
	Ellipse index	1.12 (± 0.07)	1.12 (± 0.06)	1.13 (± 0.07)	1.54 (± 0.57)
		BMO	**ASCO**	**SFO/ASCO Conjugate Opening**	**NCMCA**
Non-Hi-ESF Eyes *(n=289)*	Area (mm^2)	1.79 (± 0.36)	2.23 (± 0.43)	2.21 (± 0.44)	1.40 (± 0.38)
	Long axis (μm)	1594.72 (± 163.60)	1776.83 (± 176.22)	1772.80 (± 177.86)	1535 (± 159.08)
	Short axis (μm)	1421.21 (± 152.78)	1587.30 (± 164.75)	1578.18 (± 167.13)	1155.47 (± 248.07)
	Ellipse index	1.12 (± 0.07)	1.12 (± 0.07)	1.13 (± 0.07)	1.39 (± 0.34)
		BMO	**ASCO**	**SFO/ASCO Conjugate Opening**	**NCMCA**
Hi-ESF Eyes *(n = 73)*	Area (mm^2)	1.98 (± 0.40) ***	2.19 (± 0.42)	1.97 (± 0.36) ***	1.06 (± 0.44) ***
	Long axis (μm)	1666.58 (± 179.48) **	1753.60 (± 176.24)	1699.22 (± 177.60) **	1578.12 (± 174.04)
	Short axis (μm)	1497.70 (± 162.14) ***	1575.16 (± 153.79)	1473.25 (± 143.18) ***	845.86 (± 315.47) ***
	Ellipse index	1.11 (± 0.05)	1.11 (± 0.05)	1.16 (± 0.09) *	2.14 (± 0.84) ***

Hi-ESF data in bold yellow, (bottom row), are significantly increased or decreased in the Hi-ESF compared to the non-Hi-ESF eyes (non-paired t-test) (*** $p < 0.001$; ** $p < 0.002$; * $p = 0.01$)